



AbdulJabbar, K. et al. (2020) Geospatial immune variability illuminates differential evolution of lung adenocarcinoma. *Nature Medicine*, 26(7), pp. 1054-1062. (doi: 10.1038/s41591-020-0900-x)

There may be differences between this version and the published version. You are advised to consult the publisher's version if you wish to cite from it.

<http://eprints.gla.ac.uk/221518/>

Deposited on: 18 August 2020

Enlighten – Research publications by members of the University of Glasgow
<http://eprints.gla.ac.uk>

1 **Geospatial immune variability illuminates**
2 **differential evolution of**
3 **lung adenocarcinoma**

4 Khalid AbdulJabbar^{1,2^}, Shan E Ahmed Raza^{1,2^}, Rachel Rosenthal^{3,4#}, Mariam Jamal-Hanjani^{3,5#},
5 Selvaraju Veeriah^{3,4#}, Ayse Akarca⁶, Tom Lund⁷, David A. Moore^{3,6}, Roberto Salgado^{8,9}, Maise Al
6Bakir⁴, Luis Zapata^{1,2}, Crispin T. Hiley^{3,4}, Leah Officer¹⁰, Marco Sereno¹¹, Claire Rachel Smith¹¹,
7Sherene Loi⁹, Allan Hackshaw¹², Teresa Marafioti⁶, Sergio A. Quezada¹³, Nicholas McGranahan^{3,14},
8 John Le Quesne^{10,11,15*}, TRACERx consortium, Charles Swanton^{3,4,5*} and Yinyin Yuan^{1,2*}

9
10 ^: Joint first authors

11 #: Joint second authors

12 *: Joint corresponding authors

13
14 ¹Centre for Evolution and Cancer, The Institute of Cancer Research, London, UK

15 ²Division of Molecular Pathology, The Institute of Cancer Research, London, UK

16 ³Cancer Research UK Lung Cancer Centre of Excellence, University College London Cancer Institute,
17 London, UK

18 ⁴Cancer Evolution and Genome Instability Laboratory, The Francis Crick Institute, London, UK

19 ⁵Department of Medical Oncology, University College London Hospitals NHS Foundation Trust, 20
London, UK

21 ⁶Department of Cellular Pathology, University College London, University College Hospital, London,
22 UK

23 ⁷Translational Immune Oncology Group, Centre for Molecular Medicine, Royal Marsden Hospital
24 NHS Trust, London, UK

25 ⁸Department of Pathology, GZA-ZNA-Ziekenhuizen, Antwerp, Belgium

26 ⁹Division of Research, Peter MacCallum Cancer Centre, University of Melbourne, Melbourne, 27
Victoria, Australia

28 ¹⁰MRC Toxicology Unit, Lancaster Road, University of Cambridge, Leicester, UK

29 ¹¹Leicester Cancer Research Centre, University of Leicester, Leicester, UK

30 ¹²Cancer Research UK & University College London Cancer Trials Centre, University College London,
31 London, UK

32 ¹³Cancer Immunology Unit, University College London Cancer Institute, London, UK

33 ¹⁴Cancer Genome Evolution Research Group, University College London Cancer Institute, University
34 College London, London, UK

35 ¹⁵Glenfield Hospital, University Hospitals Leicester NHS Trust, Groby Road, Leicester, UK

35 **Abstract**

36

37 Remarkable progress in molecular analyses has improved our understanding of the
38 evolution of cancer cells towards immune escape¹⁻⁵. However, the spatial configurations
39 of immune and stromal cells, which may shed light on the evolution of immune escape
40 across tumor geographical locations, remain unaddressed. We integrated multi-region
41 exome and RNA-seq data with spatial histology mapped by deep learning in 100 non-small
42 cell lung cancer (NSCLC) patients from the TRACKing Cancer Evolution through Therapy (Rx)
43 (TRACERx) cohort⁶. Cancer subclones derived from immune cold regions were more closely
44 related in mutation space, diversifying more recently than subclones from immune hot
45 regions. In TRACERx and in an independent multi-sample cohort of 970 lung
46 adenocarcinoma (LUAD) patients, the number of immune cold regions significantly
47 correlated with risk of relapse, independently of tumor size, stage and number of samples
48 per patient. In LUAD, but not lung squamous cell carcinoma (LUSC), geometrical
49 irregularity and complexity of the cancer-stromal cell interface significantly increased in
50 tumor regions without disruption of antigen presentation. Decreased lymphocyte
51 accumulation in adjacent stroma was observed in tumors with low clonal neoantigen
52 burden. Collectively, immune geospatial variability elucidates tumor ecological constraints
53 that may shape the emergence of immune evading subclones and aggressive clinical
54 phenotypes.

55

56 **Main Text**

57

58 Using an artificial intelligence framework, we developed a generalizable deep learning
59 pipeline to spatially profile immune infiltration and discover tumor topological
60 determinants of immunosuppression in digital pathology. Convolutional neural networks
61 were tailored for the analysis of NSCLC morphology using diverse histology samples in the
62 multi-region TRACERx 100 cohort⁶ to avoid overfitting (Methods). This approach enabled
63 the spatial mapping of cancer cells, lymphocytes, stromal cells (fibroblasts and endothelial
64 cells), and an “other” cell class (macrophages, pneumocytes and non-identifiable cells) in
65 hematoxylin & eosin (H&E)-stained images (275 tumor regions from 85 patients and 100
66 diagnostic slides from all patients, Fig. 1a-c, CONSORT diagram Extended Data Fig. 1a-b,
67 Supplementary Table 1). T cell subsets were also identified in CD4/CD8/FOXP3
68 immunohistochemistry (IHC) images for all 100 diagnostic samples (Fig. 1d).

69

70 This pipeline for H&E analysis exhibited high accuracy and consistency compared with five
71 orthogonal data types within TRACERx, including DNA-seq, RNA-seq, IHC, 5,951 single-cell
72 annotations by pathologists (balanced accuracy, as an average of specificity and sensitivity
73 = 0.932), and pathology tumor-infiltrating lymphocyte (TIL) estimates following the
74 guidelines developed by the International Immuno-Oncology Biomarker Working Group⁷
75 (Extended Data Fig. 2, Supplementary Table 2). The Leicester Archival Thoracic Tumor
76 Investigatory Cohort⁸ (LATTICe-A, Extended Data Fig. 1c-d), a retrospective study of 970
77 resected LUAD patients that included H&E sections from all diagnostic tumor blocks with a
78 median of four samples per tumor, was used for independent validation. The pipeline’s
79 generalizability was supported using 5,082 pathologists’ single-cell annotations (balanced
80 accuracy = 0.913), and virtual integration of IHC and H&E images generated from the same
81 slides (Fig. 1e-h, Extended Data Fig. 2e-g, Supplementary Table 3). Using this unbiased
82 scalable approach, immune infiltration was quantified as the percentage of all cells that
83 were lymphocytes in each H&E image.

84

85 High geospatial immune variability between tumor regions within the same patients was
86 revealed (Fig. 2a-b), which did not reflect associations with pathological stage (Extended
87 Data Fig. 3). To differentiate highly from poorly immune infiltrated tumor regions, regions
88 containing a lymphocyte percentage greater than a quarter standard deviation above the
89 median lymphocyte percentage were classified as immune hot, and regions containing a
90 lymphocyte percentage below a quarter standard deviation of the median were classified
91 as immune cold. The remaining 20% were classified as intermediate (Fig. 2b). Subsequent
92 results were tested on four more classification schemes based on the standard deviation
93 to ensure that results derived from this classification were not contingent upon choice of
94 thresholds used (Extended Data Fig. 4). Significant difference in pathology TIL estimates

95 was observed between immune hot and cold regions ($R = 4.6 \times 10^{-8}$, Extended Data
96 Fig. 5a). Significantly higher levels of RNA-seq estimated immune infiltrate¹, particularly for
97 immune activation subsets, were consistently observed in immune hot compared to cold
98 regions, supporting the validity of histology-based immune classification (Fig. 2c-d). We
99 next directly compared our immune hot and cold regional classification (excluding
100 intermediate regions) against RNA-seq-based¹ classifications ($n = 109$ regions with histology
101 and RNA-seq data). 78 out of 109 regions were in agreement (Fisher's exact test for
102 overlap: $R = 7.8 \times 10^{-6}$, Extended Data Fig. 5b). Regions with discrepant classification ($n = 31$)
103 had significantly higher spatial heterogeneity of lymphocyte distribution compared
104 to regions concordant between the two methods ($R = 0.01$, Extended Data Fig. 5c),
105 suggesting spatial intratumor heterogeneity could contribute towards the discrepancy,
106 since the different data types were derived from adjacent sections of the same tumor
107 blocks.

108
109 Ecological selection pressures drive genetic divergence^{9,10}. To determine if cancer genetic
110 divergence differs according to immune context, we calculated the genomic distance as
111 the Euclidean distance of subclonal mutations for each pair of tumor regions with the
112 same immune phenotype in a patient. We observed significantly lower genomic distance,
113 indicating more shared subclonal mutations, for pairs of immune cold regions than for
114 pairs of immune hot regions in LUAD (Fig. 3a, Extended Data Fig. 4b, $R < 0.005$ for
115 all immune classification schemes), but not in LUSC (Extended Data Fig. 6a). In LUAD but
116 not LUSC, analysis of immune phenotypes mapped onto the phylogenetic trees⁶ revealed
117 that dominant clones (cancer cell fraction $\geq 75\%$, see Methods) in pairs of cold regions
118 were more closely related on the phylogenetic tree, compared to dominant clones in pairs
119 of immune hot regions (Fig. 3b). Moreover, dominant clones in hot regions almost always
120 diversified at the most recent common ancestor of the tree (13/15, 87%, Fig. 3c), in
121 contrast no such preference was observed in immune cold regions (11/23, 48%).

122
123 We investigated the impact of immune context on disease-free survival. Tumors with high
124 number of immune cold regions were at significantly increased risk of relapse that was
125 independent of the total number of regions sampled, tumor size and stage in both
126 histology types in TRACERx (Fig. 3d-e, Extended Data Fig. 6c-h). This association with
127 disease-free survival was also significant using the number of immune low regions as
128 estimated by RNAseq¹ in 64 TRACERx tumors with available RNA-seq data ($R = 0.002$,
129 Extended Data Fig. 6b). Following the genomic findings in LUAD, we sought to validate this
130 in 970 LUAD patients in the multi-sample LATTICE-A cohort, confirming the prognostic
131 value of immune cold sample count, that was also independent of the number of samples
132 per patient, tumor size and stage (Fig. 3f-g, Extended Data Fig. 6c-e). In both cohorts, the
133 number of immune cold samples per patient correlated with relapse, more significantly
134 than any other immune feature generated using deep learning, including the average and

135 variability of lymphocyte percentage per tumor, number of immune hot regions,
136 proportion of immune cold regions to the number of regions sampled, as well as CD8⁺ cell
137 percentage or CD8⁺ to CD4⁺FOXP3⁺ ratio in TRACERx diagnostic slides (Extended Data Fig.
138 6e).

139

140 Studies have revealed immunosuppressive fibroblast subsets localizing to the boundary of
141 tumor nests possibly contribute to T cell exclusion¹¹⁻¹³. Therefore, we hypothesized that
142 increased cancer-stroma physical contact may reflect stroma-modulated inhibition of
143 antitumor immune responses¹⁴⁻¹⁷. To measure the physical contact between cancer and
144 stromal cells (the majority being fibroblasts) identified by image analysis, we developed a
145 spatial measure, using fractal dimension to quantify the geographical irregularity and
146 complexity of the cancer-stromal cell interface (Methods, Fig. 4a, Extended Data Fig.
147 7a,b,e). Within the same tissue space, higher fractal dimension of cancer-stromal cell
148 interface suggests increased geometric irregularity and more extensive physical contact
149 between tumor and stromal cells than samples with a smooth interface. For both histology
150 types, fractal dimension was significantly higher in immune cold regions compared to
151 immune hot regions (Fig. 4b, Extended Data Fig. 7c). Moreover, the difference in fractal
152 dimension between immune cold and hot regions was more significant compared to the
153 difference in stromal cell percentage (both histology types combined: $R = 0.00036$,
154 effect size 0.49 for fractal dimension versus $R = 0.018$, effect size 0.38 for stromal cell
155 percentage, Extended Data Fig. 7d), suggesting the importance of stromal cell geographical
156 location rather than their quantity. This supports the hypothesis that the stroma-based
157 inhibition of immune infiltration¹⁷ may result from a specific topological pattern in the
158 form of cancer-stroma engagement.

159

160 To understand the associations of stromal-mediated immunosuppression in the context of
161 the genetic mechanisms of immune evasion, we related fractal dimension to dysfunction
162 in antigen presentation through loss of heterozygosity at the human leukocyte antigen
163 locus (HLA LOH), which has been identified as a potent immune escape mechanism^{1,18}. A
164 significantly higher fractal dimension was found in LUAD tumor regions with intact HLA
165 alleles compared with regions harboring HLA LOH (Fig. 4c, Extended Data Fig. 7f). This was
166 observed at the tumor level (see Methods for definition), independent of clonal
167 neoantigen burden ($R = 0.04$, multivariate regression, Extended Data Fig. 7h), but was not
168 observed in LUSC (Extended Data Fig. 7g, i).

169

170 Although clonal neoantigens have been associated with a cytotoxic immune response¹⁹,
171 the spatial distribution of lymphocytes in relation to clonal neoantigens remained unclear.
172 To provide sufficient spatial context for analysis of cell distribution, whole-section
173 TRACERx diagnostic H&E images, typically 10x larger than the regional samples, were used.
174 To test the relationship between lymphocyte spatial distribution and clonal neoantigens,

175 we leveraged an established method for lymphocyte spatial modeling²⁰. Each lymphocyte
176 was classified into three distinct spatial compartments: intra-tumor, adjacent-to-tumor or
177 distaltumor, based on unsupervised modeling of cancer-lymphocyte proximity (Fig. 4d). In
178 LUAD, but not LUSC, clonal neoantigens¹⁹ were found to be associated with a specific
179 immune spatial score to approximate pathology TIL estimates⁷, defined as the ratio of
180 adjacenttumor lymphocytes to stromal cells in the diagnostic H&E samples ($R =$
181 0.0074 , high clonal neoantigen defined as above median in LUAD, Fig. 4e; correlation as
182 continuous variables $Rho = 0.37$, $R = 0.035$ after multiple testing correction, Extended
183 Data Fig. 8a). By contrast, subclonal neoantigen burden did not correlate with any immune
184 score (Extended Data Fig. 8a), supporting the notion that clonal but not subclonal
185 neoantigens is associated with infiltration of cytotoxic T cells¹⁹ adjacent to tumor nests.

186

187 To determine if there was an enrichment of a specific lymphocyte subpopulation within
188 the adjacent-tumor compartment in LUAD, we spatially aligned IHC to H&E in 10 samples
189 with the highest adjacent-tumor lymphocytes to stromal cell ratio, and projected IHC-
190 derived T cell subsets onto H&E images, thereby creating virtual staining of cells in the
191 H&E sections (Methods, Fig. 4f, Extended Data Fig. 8b-c). $CD4^+FOXP3^-$, $CD8^+$, and
192 $CD4^+FOXP3^+$ cells classified in IHC were projected onto a density map of cancer cell
193 distribution inferred from H&E, and were classified into adjacent-tumor, intra-tumor, and
194 distal-tumor compartments. In this limited dataset, a significant increase of the effector-
195 regulator balance defined by $CD8^+/CD4^+FOXP3^+$ cell ratio was observed in adjacent-tumor
196 stroma compared to the distal tumor compartment (Fig. 4g).

197

198 In summary, by training deep learning algorithms in diverse histology samples, we
199 demonstrated that digital pathology can provide accurate tools for defining the ecological
200 spatial context that may improve our understanding of cancer evolution and the immune
201 response. In TRACERx and LATTICE-A cohorts, LUAD tumors with increased immune cold
202 regions were at a significantly higher risk of cancer relapse, independent of total regions
203 sampled and immune phenotypes of other regions. Thus, even within a tumor that has on
204 average increased immune infiltration, if it contains regions classified as immune cold,
205 prognosis appears to be associated with the number of cold regions. Analysis of cancer
206 branched evolution within the ecological context of immune hot and cold regions revealed
207 a difference in the evolution history of cancer subclones in these regions, possibly as a
208 result of immunoediting. Based on this finding, we speculate that by identifying the
209 subclone where immunoediting is likely to have occurred, new drivers of immune evasion
210 may be elucidated.

211

212 Spatial histology data can extend our knowledge of the tumor microenvironment
213 topological configuration in relation to genetic alterations relevant to immune
214 surveillance, including HLA LOH and clonal neoantigens in LUAD (Extended Data Fig. 9).
215 Increased cancerstromal engagement as measured by fractal dimension may signal
216 physical constraints against T cell ingress. This is supported by previous studies in lung
217 cancer showing restriction of CD8⁺ and CD4⁺ T cell motility in dense stromal extracellular
218 matrix areas around tumor epithelial cell regions which prevent them from entering tumor
219 islets¹³. Additionally, the association between specific spatial localization of lymphocytes in
220 tumoradjacent stroma and clonal neoantigens further support exploration of the role of
221 stromal cells in limiting tumor infiltration by T cells¹⁴⁻¹⁷.

222

223 It will be imperative to validate our findings on a larger multi-region cohort of untreated
224 NSCLC tumors. Differences in our findings pertaining to LUAD and LUSC may reflect
225 differences in biology²¹⁻²³ and immune evasion mechanisms, including increased
226 prevalence of antigen presentation dysfunction (HLA transcriptional repression and HLA
227 LOH¹) in LUSC. Other limitations include the lack of detailed staining using multiplexing
228 technologies²⁴⁻²⁶ that could provide further insights into immune composition. However,
229 with advanced deep learning developments and detailed tumor phylogenetic data,
230 histology can be used to highlight fundamental immune contexture such as immune
231 exclusion and its topological determinants. These data illuminate the clinical significance
232 of immune cold regions that may reflect immune evading subclones, warranting further
233 investigation into mechanisms that could contribute to the spatial variability of immune
234 cells.
235

236

237 **Figures legends**

238

239 **Figure 1. The computational pathology deep learning pipeline for dissecting**
240 **heterogeneous NSCLC tumor microenvironment. a.** Histology sample generation in Lung
241 TRACERx. To preserve morphology and generate good quality histology, samples from the
242 same tumor regional frozen blocks specifically collected for TRACERx and generated
243 molecular data^{1,6} were re-embedded in formalin fixed paraffin (FFPE). From these,
244 H&Estained tumor section slides were generated. In addition, H&E section and triplex
245 CD4/CD8/FOXP3 IHC slides were also generated from diagnostic blocks that represent
246 clinical standard sampling. **b.** Our multistage deep learning pipeline consists of three key
247 stages: fully automated tissue segmentation, single-cell detection and classification. The
248 final output is shown as an image with all cells identified. For more details, please see the
249 ‘Training the deep learning pipeline’ section of the Methods. **c.** Illustrative 3-dimensional
250 distribution of input image patches in the feature space learned by the convolutional
251 neural networks, using Principal Component Analysis. The feature clusters were pseudo-
252 colored to display segregation for four cell types in H&E, and **d** CD8⁺, CD4⁺FOXP3⁺,
253 CD4⁺FOXP3⁻ and “other” cell class (hematoxylin cells) in IHC, respectively. **e.** The deep
254 learning single-cell classification model was trained using expert pathology annotations
255 from a variety of TRACERx samples (diagnostic, regional, TMA). The trained model was
256 then applied to the remaining TRACERx samples (predominantly LUAD and LUSC) and the
257 LATTICe-A cohort (only LUAD), identifying over 171 million cells in TRACERx and over 4.9
258 billion cells in LATTICe-A. WSI: whole-section image. **f.** Biological validation of the deep
259 learning approach. H&E and IHC images generated from the same TMA slide were virtually
260 integrated for comparison of H&E-based cell classification and cell type marker expression.
261 For each marker, the experiment was conducted once using a single TMA (cores/patients
262 = 48 TTF1; 38 CD45). Scale bars represent 100µm. **g-h.** Correlations between
263 cancer/lymphocyte cell percentage determined by H&E and TTF1⁺ (tumor marker)/CD45⁺
264 (immune marker) cell percentage per LUAD image tiles of size 100µm² (= 100 TTF1;
265 83 CD45). The shading indicates 95% confidence interval.

266

267 **Figure 2. Geospatial heterogeneity of lymphocytic infiltration in the TRACERx cohort. a.**
268 Representative examples of immune hot and immune cold multi-region H&E samples,
269 scale bars represent 100µm. **b.** Each column represents a tumor, grouped by their
270 histologic subtype (the “Other” group consists of adenosquamous carcinoma, large cell
271 neuroendocrine carcinoma, pleomorphic carcinoma, and sarcomatoid carcinoma of
272 pleomorphic type arising from adenocarcinoma). Tumor regions (illustrated as dots) were
273 assigned to immune hot, immune cold, and intermediate phenotypes based on percentage
274 of lymphocytes in all cells following H&E-based deep learning analysis.
275 CD8⁺/CD4⁺FOXP3/CD4⁺FOXP3⁺ percentages based on automated analysis of the IHC

276 diagnostic samples are also shown. **c.** A heatmap showing gene expression patterns of 14
277 immune cell populations across tumor regions, each row represents a tumor region (=
278 142). The three clusters correspond to the proposed immune regional classification as
279 shown in **b.** **d.** Significant enrichment of all immune cell populations in hot regions, as
280 compared to cold regions, particularly for the immune activating cell subsets, including
281 cytotoxic, B-cell, and natural killer cells (= 109 regions; 52 patients). A two-sided, non-
282 parametric, unpaired, Wilcoxon signed-rank test was used for each box plot, all R-values
283 were corrected for multiple comparisons. Thick horizontal lines indicate the median value;
284 outliers are indicated by the extreme points; the first and third quantiles are represented
285 by the box edges; and vertical lines indicate the error range.

286

287 **Figure 3. Evolution of immune escape, and survival analysis in TRACERx and LATTICE-A.**

288 **a.** A box plot showing the difference in genomic distances for pairs of immune hot or
289 immune cold regions within the same patients in LUAD (= 66 pairs). **b.** A box plot showing
290 the difference in mutational distance between the dominant subclones in pairs of immune
291 hot or immune cold regions via their last common ancestor in LUAD (= 23 immune cold
292 pairs; 15 immune hot pairs). This distance was calculated by taking the furthest dominant
293 clone (cancer cell fraction (CCF) \geq 75%) from the trunk, and it remained significant when
294 the dominant clone closest to the most recent common ancestor of each tree was
295 considered (R = 0.02). **c.** Illustrative examples of tumor phylogenetic trees for a pair of
296 immune hot and immune cold regions. Dominant subclones were labelled and their last
297 common ancestor (annotated with arrows) was then identified. Minor (CCF < 75%) or
298 undetected clones were neglected in this analysis. **d,e.** Kaplan-Meier curves illustrating the
299 difference in disease-free survival according to the number of immune cold regions,
300 dichotomized by the median value, in TRACERx (**d**) (LUAD and LUSC, = 79 patients, 249
301 regions) and LATTICE-A (**e**) (LUAD, = 970 patients, 4,324 samples). The same deep learning
302 histology analysis and immune regional classification developed for TRACERx were applied
303 directly to LATTICE-A. WSI: whole-section image. **f.** Forest plots showing multivariate Cox
304 regression analyses in TRACERx (= 79 patients; LUAD and LUSC). Clonal neoantigens were
305 dichotomized using the upper quartile, determined individually for LUAD and LUSC
306 tumors¹. **g.** Forest plots showing multivariate Cox regression analyses in LATTICE-A (= 651
307 LUAD patients with complete stage and smoking pack years data). For the patient subset
308 with complete stage data but missing pack years information, the test remained significant
309 (= 827, R < 0.001, HR = 1.4[1.1-1.9]). For statistical comparisons among groups, a
310 two-sided, non-parametric, unpaired, Wilcoxon signed-rank test was used, unless stated
311 otherwise.

312

313 **Figure 4. Association of spatial histology with genetic alterations relevant to immune**
314 **surveillance. a.** An illustrative example of fractal dimension calculated by the box-counting

315 algorithm to quantify the geospatial complexity of the cancer cell-stromal cell interface. By
316 examining boxes of decreasing sizes that contain both cancer and stromal cells, the box
317 counting algorithm quantifies the rate at which the geometrical details of cancer-stromal
318 interface develop at increasingly fine scales. Blue box illustrates the smallest box of 20 μ m
319 by
320 20 μ m in size. Scale bar represent 100 μ m. An example of a fractal structure displaying
321 geometrical self-similarity is shown below the panel. **b.** A box plot to illustrate the
322 significant difference in fractal dimension between all TRACERx immune hot and cold
323 regions (= 219).
324 **c.** A box plot showing a significant difference in fractal dimension between LUAD tumor
325 regions (= 116) harboring an LOH event for class 1 HLA of any type versus regions that do
326 not, adjusted for multiple comparisons with the remaining HLA type-specific tests (see
327 Extended Data Fig. 7f). **d.** Illustration of the adjacent-tumor lymphocyte/stroma ratio
328 inferred by spatial modeling of cancer cell density (contours) and lymphocyte classification
329 into spatial compartments. Cell classification in IHC sample of the same block was shown
330 for comparison. Scale bars represent 50 μ m. **e.** A box plot showing the difference in the
331 adjacent-tumor lymphocyte/stroma ratio between high (\geq median) and low ($<$ median)
332 clonal neoantigens for all LUAD patients in TRACERx (= 61). **f.** Illustration of image
333 registration to spatially align serial sections of H&E and IHC and generate a virtual
334 composite map of T cell subset in the context of cancer/stroma density. T cell subsets
335 classified in the IHC were projected onto the cancer density map inferred from H&E, so
336 that they can be classified into adjacent-tumor, intra-tumor, and distal-tumor
337 compartments. **g.** A box plot showing significantly higher ratio of CD8⁺ to CD4⁺FOXP3⁺ cells
338 in adjacent-tumor and intratumor lymphocytes compared with distal-tumor lymphocytes
339 in registered LUAD image tiles (= 20 image tiles, using paired Wilcoxon test). For statistical
340 comparisons among groups, a two-sided, non-parametric, unpaired, Wilcoxon signed-rank
341 test was used, unless stated otherwise.

342

343

344 **Main References**

345

- 346 1. Rosenthal, R. et al. Neoantigen-directed immune escape in lung cancer evolution.
347 Nature 1 (2019). doi:10.1038/s41586-019-1032-7
- 348 2. Morris, L. G. T. & Chan, T. A. Lung Cancer Evolution: What's Immunity Got to Do
349 with It? Cancer Cell 35, 711–713 (2019).
- 350 3. Morris, L. G. T. et al. Pan-cancer analysis of intratumor heterogeneity as a
351 prognostic determinant of survival. Oncotarget 7, 10051–10063 (2016).

- 352 4. Milo, I. et al. The immune system profoundly restricts intratumor genetic
353 heterogeneity. *Sci. Immunol.* 3, (2018).
- 354 5. Jia, Q. et al. Local mutational diversity drives intratumoral immune heterogeneity in
355 non-small cell lung cancer. *Nat. Commun.* 9, (2018).
- 356 6. Jamal-Hanjani, M. et al. Tracking the Evolution of Non–Small-Cell Lung Cancer. *N.*
357 *Engl. J. Med.* 376, 2109–2121 (2017).
- 358 7. Hendry, S. et al. Assessing Tumor-Infiltrating Lymphocytes in Solid Tumors. *Adv.*
359 *Anat. Pathol.* 24, 311–335 (2017).
- 360 8. Moore, D. A. et al. In situ growth in early lung adenocarcinoma may represent
361 precursor growth or invasive clone outgrowth—a clinically relevant distinction.
362 *Mod. Pathol.*
363 1 (2019). doi:10.1038/s41379-019-0257-1
- 364 9. Whittaker, K. A. & Rynearson, T. A. Evidence for environmental and ecological
365 selection in a microbe with no geographic limits to gene flow. *Proc. Natl. Acad. Sci. U. S. A.*
366 114, 2651–2656 (2017).
- 367 10. Shafer, A. B. A. & Wolf, J. B. W. Widespread evidence for incipient ecological
368 speciation: A meta-analysis of isolation-by-ecology. *Ecology Letters* 16, 940–950 (2013).
- 369 11. Costa, A. et al. Fibroblast Heterogeneity and Immunosuppressive Environment in
370 Human Breast Cancer. *Cancer Cell* 33, 463-479.e10 (2018).
- 371 12. Öhlund, D. et al. Distinct populations of inflammatory fibroblasts and
372 myofibroblasts in pancreatic cancer. *J. Exp. Med.* 214, 579–596 (2017).
- 373 13. Salmon, H. et al. Matrix architecture defines the preferential localization and
374 migration of T cells into the stroma of human lung tumors. *J. Clin. Invest.* 122, 899–910
375 (2012).
- 376 14. Thomas, D. A. & Massagué, J. TGF- β directly targets cytotoxic T cell functions
377 during tumor evasion of immune surveillance. *Cancer Cell* 8, 369–380 (2005).
- 378 15. Joyce, J. A. & Fearon, D. T. T cell exclusion, immune privilege, and the tumor
379 microenvironment. *Science* (80-.). 348, 74–80 (2015).
- 380 16. Sorokin, L. The impact of the extracellular matrix on inflammation. *Nat. Rev.*
381 *Immunol.* 10, 712–723 (2010).
- 382 17. Chen, D. S. & Mellman, I. Elements of cancer immunity and the cancer–immune set
383 point. *Nature* 541, 321–330 (2017).
- 384 18. McGranahan, N. et al. Allele-Specific HLA Loss and Immune Escape in Lung Cancer
385 Evolution. *Cell* 171, 1259-1271.e11 (2017).
- 386 19. McGranahan, N. et al. Clonal neoantigens elicit T cell immunoreactivity and
387 sensitivity to immune checkpoint blockade. *Science* (80-.). 351, (2016).
- 388 20. Yuan, Y. Modelling the spatial heterogeneity and molecular correlates of
389 lymphocytic infiltration in triple-negative breast cancer. *J. R. Soc. Interface* 12, 20141153
390 (2015).

- 391 21. Thomas, A., Liu, S. V., Subramaniam, D. S. & Giaccone, G. Refining the treatment of
392 NSCLC according to histological and molecular subtypes. *Nat. Rev. Clin. Oncol.* 12, 511–526
393 (2015).
- 394 22. Hammerman, P. S. et al. Comprehensive genomic characterization of squamous
395 cell lung cancers. *Nature* 489, 519–525 (2012).
- 396 23. Collisson, E. A. et al. Comprehensive molecular profiling of lung adenocarcinoma:
397 The cancer genome atlas research network. *Nature* 511, 543–550 (2014).
- 398 24. Keren, L. et al. A Structured Tumor-Immune Microenvironment in Triple Negative
399 Breast Cancer Revealed by Multiplexed Ion Beam Imaging. *Cell* 174, 1373-1387.e19 (2018).
- 400 25. Giesen, C. et al. Highly multiplexed imaging of tumor tissues with subcellular
401 resolution by mass cytometry. *Nat. Methods* 11, 417–422 (2014).
- 402 26. Goltsev, Y. et al. Deep Profiling of Mouse Splenic Architecture with CODEX
403 Multiplexed Imaging. *Cell* 174, 968-981.e15 (2018).
- 404
- 405

406

407 **Acknowledgements**

408 This study is funded by a Cancer Research UK Career Establishment Award to Y.Y.
409 (C45982/A21808). The TRACERx study (Clinicaltrials.gov no: NCT01888601) is sponsored by
410 University College London (UCL/12/0279) and has been approved by an independent
411 Research Ethics Committee (13/LO/1546). TRACERx is funded by Cancer Research UK
412 (C11496/A17786) and coordinated through the Cancer Research UK and UCL Cancer Trials
413 Centre. Y.Y. acknowledges additional support from Breast Cancer Now (2015NovPR638),
414 Children's Cancer and Leukaemia Group (CCLGA201906), NIH U54 CA217376 and R01
415 CA185138, CDMRP Breast Cancer Research Program Award BC132057, European
416 Commission ITN (H2020-MSCA-ITN-2019), Wellcome Trust (105104/Z/14/Z), and The Royal
417 Marsden/ICR National Institute of Health Research Biomedical Research Centre. C.S. is
418 Royal Society Napier Research Professor. This work was supported by the Francis Crick
419 Institute that receives its core funding from Cancer Research UK (FC001169,FC001202),
420 the UK Medical Research Council (FC001169, FC001202), and the Wellcome Trust
421 (FC001169, FC001202). C.S. is funded by Cancer Research UK (TRACERx, PEACE and CRUK
422 Cancer Immunotherapy Catalyst Network), the CRUK Lung Cancer Centre of Excellence,
423 the Rosetrees Trust, NovoNordisk Foundation (ID16584) and the Breast Cancer Research
424 Foundation (BCRF). This research is supported by a Stand Up To Cancer-
425 LUNGeVityAmerican Lung Association Lung Cancer Interception Dream Team Translational
426 Research Grant (Grant Number: SU2C-AACR-DT23-17). Stand Up To Cancer is a program of
427 the Entertainment Industry Foundation. Research grants are administered by the
428 American Association for Cancer Research, the Scientific Partner of SU2C. CS receives
429 funding from the European Research Council (ERC) under the European Union's Seventh
430 Framework Programme (FP7/2007-2013) Consolidator Grant (FP7-THESEUS-617844),
431 European Commission ITN (FP7-PloidyNet 607722), an ERC Advanced Grant (PROTEUS)
432 from the European Research Council under the European Union's Horizon 2020 research
433 and innovation programme (grant agreement No. 835297), and Chromavision from the
434 European Union's Horizon 2020 research and innovation programme (grant agreement
435 665233). S.A.Q. is funded by a Cancer Research UK Senior Cancer Research Fellowship
436 (C36463/A22246) and a Cancer Research UK Biotherapeutic Program Grant
437 (C36463/A20764). S.L. is supported by the National Breast Cancer Foundation of Australia
438 Endowed Chair and the Breast Cancer Research Foundation, New York. L.Z. has received
439 funding from the European Union's Horizon 2020 research and innovation programme
440 under the Marie Skłodowska-Curie grant agreement No 846614. C.T.H. is funded by the
441 UCL Biomedical Research Council. M.J.H. has received funding from Cancer Research UK,
442 National Institute for Health Research, Rosetrees Trust and UKI NETs. We thank the
443 members of the TRACERx and PEACE consortia for participating in this study. We thank the
444 Tissue Image Analytics lab at the University of Warwick, Coventry, UK for their help in
445 method implementation. We thank the Scientific Computing team at The Institute of

446 Cancer Research, London for technical support. We also thank Ana Teodósio and Catherine
447 Ficken from the MRC Toxicology Unit core histology facility for their expert technical
448 assistance.

449

450 **Author Contributions**

451 K.A. and S.E.A.R. contributed equally to this work. S.E.A.R. and K.A. developed the image
452 processing and deep learning pipeline and performed the geospatial analysis. K.A.
453 performed the bioinformatics and statistical analyses. J.L.Q., R.S. and D.A.M. provided
454 pathological expertise. M.J.-H. provided clinical expertise and patient characterization. S.V.
455 performed histology sample generation and digitized H&E slides. A.A. generated and
456 digitized IHC slides under the supervision of T.M. T.L. provided annotations for training and
457 validating IHC analysis. N.M., R.R. and L.Z. assisted with genomic data integration. J.L.Q.,
458 R.S., S.L., M.A.B., D.A.M., C.T.H., and T.L. analyzed pathology TIL estimates. J.L.Q., L.O.,
459 M.S., and C. R. S. provided data and advice for LATTICe-A. Y.Y., N.M., J.L.Q., C.S., A.H. and
460 S.A.Q. provided data analysis support and supervision. K.A., R.R., N.M., C.S. and Y.Y. wrote
461 the manuscript with input from all authors. Y.Y. and C.S. jointly conceived and supervised
462 the study.

463

464 **Competing Interests**

465 Y.Y. has received speakers bureau honoraria from Roche and is a consultant for Merck and
466 Co Inc. C.S. receives grant support from Pfizer, AstraZeneca, BMS, Roche-Ventana,
467 Boehringer-Ingelheim and Ono Pharmaceutical. C.S. has consulted for Pfizer, Novartis,
468 GlaxoSmithKline, MSD, BMS, Celgene, AstraZeneca, Illumina, Genentech, Roche-Ventana,
469 GRAIL, Medicxi, and the Sarah Cannon Research Institute. C.S. is a shareholder of Apogen
470 Biotechnologies, Epic Bioscience, GRAIL, and has stock options in and is co-founder of
471 Achilles Therapeutics. M.A.B. is a consultant for Achilles Therapeutics. S.L. receives
472 research funding to her institution from Novartis, Bristol Meyers Squibb, Merck, Roche-
473 Genentech, Puma Biotechnology, Pfizer, Eli Lilly and Seattle Genetics. S.L. has acted as
474 consultant (not compensated) to Seattle Genetics, Pfizer, Novartis, BMS, Merck,
475 AstraZeneca and RocheGenentech. S.L. has acted as consultant (paid to her institution) to
476 Aduro Biotech, Novartis, and G1 Therapeutics. D.A.M. has received speaker's fees from
477 AstraZeneca. M.J.H. is a member of the Advisory Board for Achilles Therapeutics.

478

479 **Materials and Correspondence**

480 Materials request and general correspondence should be addressed to J.L.Q., C.S. and Y.Y.

481

482 **Data availability**

483 The digital pathology images from the TRACERx study generated or analysed during this
484 study are not publicly available and restrictions apply to its use. A test subset of such

485 digital pathology images are available through the Cancer Research UK & University
486 College London Cancer Trials Centre (ctc.tracerx@ucl.ac.uk) for non-commercial research
487 purposes and access will be granted upon review of a project proposal that will be
488 evaluated by a TRACERx data access committee and entering into an appropriate data
489 access agreement, subject to any applicable ethical approvals. Digital pathology images for
490 LATTICe-A samples with expert pathologist's annotations used for validation are available:
491 <https://github.com/qalid7/compath>. Request for data access for the remaining LATTICe-A
492 samples can be submitted to J.L.Q.

493

494 **Code availability**

495 The deep learning pipeline for digital pathology image analysis is available for
496 noncommercial research purposes: <https://github.com/qalid7/compath>. All code used for
497 statistical analyses of image data was developed in R version (3.5.1) and is available:
498 https://github.com/qalid7/tx100_compath.

499

500
501
502

Methods

Tissues and digital images

503 The main cohort evaluated comes from the first 100 patients prospectively analyzed by the
504 lung TRACERx study⁶ (Extended Data Fig. 1, Supplementary
505 Tables 1, 4, <https://clinicaltrials.gov/ct2/show/NCT01888601>, approved by an
506 independent Research Ethics Committee, 13/LO/1546). 62 were men and 38 were women,
507 with a median age of 68. 61 were LUAD, 32 were LUSC and the remaining 7 had 'other'
508 histology subtypes (including adenosquamous carcinoma, large cell carcinoma, large cell
509 neuroendocrine carcinoma, pleomorphic carcinoma and pleomorphic
510 carcinoma arising from adenocarcinoma).
511

512

513 The 85 case subcohort with regional histology consisted of 55 male and 30 female patients
514 and of those 49 were LUAD, 32 were LUSC and 6 were 'other' types. 10 of these patients
515 had a single region while the rest ranged between 2-8 regions (= 275 total regional
516 histology samples). Snap-frozen regional samples were processed to FFPE blocks after
517 dissecting fresh-frozen tissues for DNA-seq and RNA-seq analyses. Tissue microarrays
518 (TMAs) were created containing 133x2mm regional tissue cores from 75 patients in 7
519 blocks.

520

521 In addition to the regional samples, full-sized diagnostic blocks were obtained for all 100
522 cases precisely mirroring the Jamal-Hanjani et al. 2017 prospective 100 patient cohort⁶.
523 4µm thick sections were cut and subjected to H&E staining and multiplex IHC for
524 CD8/CD4/FOXP3: anti-CD8 (type: Rabbit Monoclonal, clone: SP239, cat. no.: ab178089,
525 source: Abcam Plc, Cambridge, UK, used at 1:100); anti-CD4 (type: Rabbit Monoclonal,
526 clone: SP35, cat. no.: ab213215, source: Abcam Plc, Cambridge, UK, used at 1:50);
527 antiFOXP3 (type: Mouse, clone: 236A/E7, source: kind gift from Dr G Roncador, CNIO,
528 Madrid, Spain, used at: 1:100). All regional and diagnostic slides were scanned using
529 NanoZoomer S210 digital slide scanner (C13239-01) and NanoZoomer digital pathology
530 system version
531 3.1.7 (Hamamatsu, Japan) at 40x (228 nm/pixel resolution).
532

532

533 The external validation cohort was obtained from the Leicester Archival Thoracic Tumor
534 Investigatory Cohort – Adenocarcinoma (LATTICE-A) study⁸, a continuous retrospective
535 series of resected primary LUAD tumors from a single surgical center between years 1998
536 to 2014 (Extended Data Fig. 1, Supplementary Table 5). It consists of 4,324 whole-tumor
537 diagnostic blocks from 970 LUAD patients (ranging from 1 to 16 blocks per case with a
538 median of 4). 455 were men and 515 were women with a median age of 69. Most clinical
539 data (age, sex, adjuvant therapy status and time to recurrence or death) were available for

540 all patients, with complete pathological stage for 827 and smoking history for 651. All
541 archival slides containing tumor material were used in order to capture the full diversity of
542 each lesion. Slides were dearchived and scanned using a Hamamatsu NanoZoomer XR at
543 40x (226 nm/pixel resolution) yielding 15 TB of image data. Images containing incidental
544 lymph node tissue were excluded to avoid confounding immune infiltration analysis. For
545 the biological validation assay, a subset of 49 paraffin blocks from 49 patients was
546 obtained from the same study, and from these a validation TMA was prepared, containing
547 a single 1mm core from each case. The work was ethically approved by an NHS research
548 ethics committee (ref. 14/EM/1159). This study complies with the STROBE guidelines.

549

550 **The deep learning pipeline for cell detection and classification**

551 The deep learning pipeline consists of three parts. First, the pipeline segments tissue
552 regions utilizing multi-resolution input/output image features (Micro-Net²⁷). It was
553 designed to capture global tissue context and learn weak features that could be important
554 for identifying tissue boundary, but are often not achieved by other machine learning
555 methods such as thresholding of the grey-scale image, active contours, watershed
556 segmentation or Support Vector Machine-based training on local binary pattern features²⁷.
557 Tissue segmentation removes background noise and artefacts and subsequently allows for
558 more computationally efficient cell detection and accurate classification. Secondly, a cell
559 detection model modified from SCCNN²⁸ predicts for each pixel the probability that it
560 belongs to the center of a nucleus within tissue regions identified by Micro-Net. Nuclei are
561 detected from the probability map obtained from the deep network. Lastly, a cell
562 classification framework utilizes a neighboring ensemble predictor classifier coupled with
563 SCCNN to classify each cell by type.

564

565 For tissue segmentation, each whole slide image was reduced to 1.25x resolution and
566 segmented for tissue regions using Micro-Net-512²⁷ architecture. This architecture
567 visualizes the image at multiple resolutions, captures context information by connecting
568 intermediate deep layers and adds bypass connections to max-pooling to maintain weak
569 features (Fig. 1b). 10 whole slide images were used to train the tissue segmentation
570 network using MicroNet. The segmented images from the network were inspected visually
571 and quantitatively (Supplementary Table 6, Supplementary Figures 1-20) to evaluate
572 performance using an independent set of images.

573

574 The SCCNN adds two layers to conventional deep learning architecture for cell detection
575 within the segmented tissue. SC1 estimates the location and probability of each pixel
576 belonging to the center of a cell, and these probabilities are then mapped by SC2 to the
577 image. A customized implementation of SCCNN was coded in Python (version 3.5) using
578 TensorFlow²⁹ library (version 1.3) which makes it computationally more efficient
579 compared to the original MATLAB implementation²⁸. To process an image of size

580 1000×1000 pixels, the Python implementation takes 4.8 seconds for nucleus detection
581 compared to 41.0 seconds using the original implementation²⁸, excluding preprocessing
582 which remained the same in both implementations (using MATLAB (version 2018b)). In
583 addition, through empirical experimentation, we optimized the patch size to 31×31 instead
584 of 27×27 in the original implementation for increased cell detection accuracy. To generate
585 nuclear locations from the SC2 probability map, peak detection was applied where
586 thresholds for intensity and minimum grouping distance were also optimized to 0.15 and
587 12 pixels through experimentation using validation data.

588

589 For cell classification, a neighboring ensemble predictor was used. This predictor utilizes
590 SCCNN to classify cells in neighboring locations to the detected center of the cell. In our
591 implementation, the ensemble classifier required votes from SCCNN classification of nine
592 different neighborhood locations near to the center of the cell compared to five votes in
593 original implementation. Through experimentation, the patch size was optimized to 51×51
594 for classification instead of 27×27 as originally proposed. This permitted incorporation of
595 greater tissue spatial context while maintaining the accuracy of classifying small cells.

596

597 Altogether, this pipeline enabled the spatial mapping of four cell types from H&E images:
598 cancer (malignant epithelial) cells, lymphocytes (including plasma cells), non-inflammatory
599 stromal cells (fibroblasts and endothelial cells), and an “other” cell type that included
600 nonidentifiable cells, less abundant cells such as macrophages and chondrocytes, and
601 ‘normal’ pneumocytes and bronchial epithelial cells.

602

603 **Training the deep learning pipeline**

604 To improve neural network generalizability and to avoid overfitting for cell detection and
605 classification, we trained and tested our pipeline on a variety of sample types, including
606 diagnostic (= 100), regional (= 275) and 133 cores corresponding to 75 TRACERx patients
607 from TMA slides (63 patients had two cores and 12 patients had a single core). Both cell
608 detection and classification were trained based on single-cell annotations from
609 pathologists. Two thoracic pathologists annotated 26,960 cells on 53 whole slide images (3
610 TMAs, 35 regional slides and 15 diagnostic slides) to incorporate morphological variations
611 in appearance of various cell types and stain variability. Several hundred examples of each
612 cell class were marked on 76 cores selected at random from TMA images. In total, 4,056,
613 5,310, 15,007, 2,587 annotations were collected for stromal cells, lymphocytes, cancer
614 cells and “other” cell types, respectively. These whole slide images were divided into small
615 tile images of size 2000×2000 pixels (each pixel = 0.5µm), which were then divided into
616 three sample sets maintaining the class distribution of cells. These included: 13 diagnostic,
617 58 regional and 134 TMA tile images for training; 4 diagnostic, 21 regional and 72 TMA tile
618 images for validation; and 3 diagnostic, 22 regional and 61 TMA tile images for testing. As

619 a result, the annotations were divided between the three groups; 2/3 for training, 1/6 for
620 validation and 1/6 for testing. The training set included annotations for 2,147 stromal cells,
621 3,183 lymphocytes, 10,103 cancer and 1,357 other cell types. The validation set had
622 annotations for 473 stromal cells, 825 lymphocytes, 2,562 tumor and 359 other cell types.
623 Breakdown for the test set is provided in Supplementary Table 2.

624
625 For IHC cell classification, we used a pretrained SCCNN network on samples stained for
626 CD4/CD8/FOXP3. The training set consisted of 1,657 CD4⁺FOXP3⁻, 3,187 CD8⁺, 1,001
627 CD4⁺FOXP3⁺, and 3,488 other (negative) cells. The trained network was tested on 5,028
628 cell annotations collected on 6 lung diagnostic whole slide images, including 251
629 CD4⁺FOXP3⁻, 406 CD8⁺, 123 CD4⁺FOXP3⁺ and 4,248 other cells to test the ability of the
630 algorithm in correctly detecting and classifying negative cells. See Supplementary Table 7
631 for the total number of identified cells in the H&E diagnostic, H&E multi-region and IHC
632 diagnostic datasets.

633

634 **Validation of the H&E deep learning pipeline with orthogonal data types**

635 The algorithms' performance in detecting and classifying single cells in H&E were first
636 evaluated against the test set of 5951 cells. Individual class accuracy statistics were
637 calculated using the R function 'confusionMatrix' from the R package 'caret'.

638

639 Pathology TIL estimates were scored following the international guidelines developed by
640 the International Immuno-Oncology Biomarker Working Group⁷. Briefly, by inspection of
641 H&E slide of a given tumor region, the fraction of the stromal area infiltrated by TILs was
642 assessed.

643

644 For regional samples, tumor cellularity, estimated as the computed percentage cancer cells
645 was correlated with tumor purity estimated by ASCAT based on DNA-seq copy number and
646 VAF purity (both available from Jamal-Hanjani et al.⁶, = 239 regional tumor samples). The
647 RNA-seq-based CD8⁺ T cell signature (available from Rosenthal et al.¹, computed using the
648 Danaher et al. method³⁰) was correlated with the deep learning based lymphocyte
649 percentage for 142 regional tumor samples. For diagnostic samples, deep learning-based
650 lymphocyte percentage from H&E was correlated with deep learning-based CD8⁺ cell
651 percentage from IHC (= 100 diagnostic samples, Extended Data Fig. 2a-d).

652

653 Discordance rate between RNA-seq based¹ and histology/deep learning-based immune hot
654 and cold regional classification was calculated by cross-tabulation of immune hot and cold
655 (from histology) versus high and low (from RNA-seq), disregarding any regions without one
656 of these two types of data. The RNA-seq method used 15 immune cell signatures
657 presenting different T- and B-cell subsets, as well as neutrophils, macrophages, mast and

658 dendritic cells, to classify tumor regions into high and low categories. A Fisher's exact test
659 was used to compute the overlap between the two immune classifications. Distributions of
660 multiple immune scores (lymphocyte percentage, intra-tumor lymphocytes and adjacent-
661 tumor lymphocytes/stroma) as well as ASCAT tumor purity were compared between hot
662 versus cold (deep learning) and high versus low (RNA-seq) classifications (Extended Data
663 Fig. 5).

664

665 **Validation of the deep learning pipeline with the independent LATTICE-A cohort**

666 The external validity of the proposed deep learning pipeline was performed on 100
667 randomly selected patients from the LATTICE-A cohort⁸. This validation ensures that the
668 trained cell detection and cell classification models from the TRACERx tumor blocks are
669 generalizable to a distinct dataset which is processed, stained and scanned in another
670 center (the LATTICE-A study, University of Leicester).

671

672 All 100 whole-tumor H&E sections were processed using the same TRACERx trained model.
673 The validation was then performed using two data types. First, a pathologist provided
674 5,082 single-cell annotations following the same protocol for TRACERx in 20 randomly
675 selected LATTICE-A sections. The breakdown for single-cell annotations was 1,997 stromal
676 cells, 787 lymphocyte cells, 1,839 cancer cells and 459 other cells (see Supplementary
677 Table 3). Second, two independent pathologists jointly scored the remaining 80 sections
678 for overall fraction of lymphocytic infiltration and pathology TIL estimates⁷. These manual
679 scores were correlated with the deep learning-based lymphocyte percentage and
680 adjacent-tumor lymphocytes/total stroma (Extended Data Fig. 2e).

681

682 **Validation of the deep learning pipeline with biological assays**

683 A new biological validation method was developed to overcome the challenge of obtaining
684 large quantities of cell-specific validation data (Fig. 1f-h, Extended Data Fig. 2f-g). 48 cores
685 were available for the TTF1-H&E image pairs, 38 for the CD45-H&E pairs, and 33 for the
686 SMA-H&E pairs. Stains were performed using a Ventana BenchMark ULTRA instrument
687 (H&E, TTF-1) or a Dako Link 48 (CD-45, SMA). Digital images were acquired using a
688 Hamamatsu Nanozoomer slide scanner. First, H&E staining was performed using a Leica
689 Infinity kit, and a digital image was collected. The slide was subsequently de-coverslipped,
690 the H&E stain removed by acid alcohol washing, and then an immunohistochemical stain
691 with haematoxylin counterstain was applied using a standard diagnostic antigen retrieval
692 and antibody protocol. A second digital image was acquired after mounting and
693 coverslipping. Through experimentation, no difference in the staining was observed when
694 the procedure was reversed.

695

696 TTF-1 (type: Novocastra Liquid Mouse Monoclonal antibody thyroid transcription factor 1,
697 clone: SPT24, cat. no.: NCL-L-TTF-1, source: Leica biosystems, Germany, used at 1:100) was
698 selected as the cancer cell marker in these LUAD samples because it is the most robust and
699 widely used immunohistochemical marker of LUAD cells³¹. It is very specific, both in that
700 only epithelial cells are stained in the lung, and in that very few tumors of non-lung or
701 thyroid origin are stained³². The sensitivity of the antibody clone used (SPT24) is also high,
702 staining >75% of tumor cells in 76% of LUAD tumors in one published series³³. However, as
703 this implies, there are many tumors in which tumor cell staining is incomplete (i.e. <100%).
704 Therefore, only cores showing near-universal TTF-1-positivity of tumor cells were used for
705 validation, in order to provide the best possible 'gold standard' comparator for the deep
706 learning algorithm. The same procedure was followed for pairs of H&E-CD45 (anti-human
707 CD45, type: Mouse Monoclonal, clone: 2B11 + PD7/26, cat. no.: M0701, source: Agilent
708 DAKO, USA, used at 1:200) and H&E-SMA (myofibroblast marker, type: Mouse Monoclonal
709 antibody Smooth Muscle Actin (1A4), cat. no.: 760-2833, source: Roche, Switzerland, a
710 ready to use antibody) to biologically validate the accuracy of single cell classification.

711

712 In total, 64,976 TTF1⁺ cells, 26,284 CD45⁺ cells and 46,343 SMA⁺ cells were detected from
713 the IHC images, denoting the advantage of this method in acquiring large amount of
714 validation data at single-cell resolution. The correlation measured (Fig. 1f-h, Extended Data
715 Fig. 2g) was that between the fraction of classified cells in the H&E versus fraction of
716 positively stained IHC cells per 100 μm^2 .

717

718 **Immune phenotype classification**

719 To classify tumor regions into different immune phenotypes, we assigned each region to
720 an immune hot, cold or intermediate category based on lymphocyte percentage. The
721 dependency of our subsequently results on thresholds chosen for this classification
722 scheme was tested after applying perturbations to the thresholds used. Four new
723 classification schemes were tested: no intermediate zone (i.e. using median lymphocyte
724 percentage for separating hot and cold regions), regions with lymphocyte percentage
725 greater than standard deviation/2 above/below the median lymphocyte percentage
726 classified as immune hot/cold, , and similarly for standard deviation/3 and standard
727 deviation/6 (Extended Data Fig. 4a-b). For every new classification, we repeated the
728 multivariate survival analysis to confirm the significance of the number of immune cold
729 regions in predicting disease-free survival as well as the genomic distance test for pairs of
730 immune hot versus immune cold regions in LUAD patients (Extended Data Fig. 4b). In
731 addition, the CD8⁺ RNA-seq signature was used to test the difference in CD8⁺ levels
732 between immune hot and immune cold phenotypes across all classification schemes
733 (Extended Data Fig. 4c).

734

735 **Genomic distance measure**

736 Genomic distance was calculated as described previously¹, by taking the Euclidean
737 distance of the mutations present for every pair of immune hot and immune cold regions
738 from the same patient. All mutations present in a region from a tumor were turned into a
739 binary matrix of which the rows were mutations and columns were the tumor regions.
740 From this matrix, the pairwise distance was determined.

741

742 **Distance between dominant clones to the last common ancestor of region pair**

743 Deep learning-based immune phenotypes were integrated with the TRACERx
744 phylogenetics data⁶. Dominant clones (using the upper quartile of cancer cell fraction, \geq
745 75%) were labelled for all tumor regions' trees which had an available H&E sample in LUAD
746 patients (= 76 regions, 15 immune hot pairs and 23 immune cold pairs). For every pair of
747 immune hot / cold regions within a tumor, the distance between the dominant clones (as
748 measured by branch length, i.e. number of mutations) via their last common ancestor was
749 computed. The recently shared ancestry clone between the two dominant clones was
750 labelled as the 'last common ancestor of region pair' (annotated with arrows in Fig 3.c). To
751 ensure this analysis was not dependent on a certain cancer cell fraction threshold, multiple
752 thresholds (CCF \geq 80%, 85%) were placed while repeating the same analysis. Next, by
753 identifying the last common ancestral subclone for pairs of the same phenotype, each pair
754 was categorized into one of two diversification patterns: 'diversifying at the most recent
755 common ancestor (MRCA) of the tree' or 'diversifying at a descendant subclone of the
756 MRCA of the tree'. The latter category included a pattern exclusive to immune cold pairs,
757 where the two regions shared the same dominant subclone that was the direct
758 descendant of the MRCA of the tree.

759

760 **Tumor spatial modelling**

761 H&E and IHC cell abundance scores (e.g. lymphocyte percentage, CD8⁺ percentage) were
762 computed as the percentage of a cell type in the total sample cell count. Stromal TILs were
763 identified using spatial modelling^{20,34,35}, where lymphocytes were classified (using
764 unsupervised clustering) into intra-tumor lymphocytes, adjacent-tumor lymphocytes and
765 distal-tumor lymphocytes based on their spatial proximity to epithelial cell nests in H&Es.
766 The immune hotspot score was calculated using the Getis–Ord algorithm as previously
767 described³⁶. To capture the emergence of complex morphological patterns that dictate
768 cancer-stromal cell spatial contact preserved over varying spatial scales, a fractal
769 dimension calculation (Minkowski-Bouligand dimension) was performed using the box-
770 counting algorithm³⁷. This algorithm calculates the number of boxes of a certain size
771 needed to cover a geometric pattern. We modified a MATLAB-based algorithm³⁸ to include
772 both spatial information of cancer and stromal cells, as opposed to its conventional use on
773 one variable (i.e. pixel information of an image). The analysis was carried out on spatial

774 maps generated using coordinates of classified stromal and cancer cells, while utilizing the
775 tissue segmented image (as a boundary mask) to exclude all empty tissue areas. Choices of
776 box size were informed by the distribution of minimum and maximum Euclidean distance
777 for each stromal cell to its nearest cancer cell in all 275 tumor regions (Extended Data Fig.
778 7a). The mean minimum distance was 21.43 μm . We limited the upper box size at 300 μm ,
779 which is just above a previously proposed cell-cell communication distance of 250 μm ³⁹ but
780 designed to be more inclusive. For statistical tests where fractal dimension was
781 represented at tumor level, the maximum regional score was used.

782

783 **H&E-IHC spatial alignment/immune subset projection**

784 For a H&E diagnostic slide, we determined the number of intra-tumor lymphocytes,
785 adjacent-tumor lymphocytes and distal-tumor lymphocytes (n_i , n_a , n_o) based on spatial
786 modelling of the H&Es. After spatial alignment of IHC and projecting IHC-derived cells onto
787 the H&E, the number of CD8⁺ cells that were also intra-tumor lymphocytes was
788 determined (n_{ITL}^{CD8}), and similarly for other cell types. As a result, intra-tumor lymphocytes
789 were deconvoluted by $n_i = n_{ITL}^{CD8} + n_{ITL}^{CD4} + n_{ITL}^{FOXP3} + n_{ITL}^{other}$. Two-sided paired Wilcoxon was used to test
790 the difference in the percentage of CD8⁺ cells among intra-tumor lymphocytes, adjacent-
791 tumor lymphocytes and distal-tumor lymphocytes (n_{ATL}^{CD8} , n_{DTL}^{CD8} , n_{ITL}^{CD8}). The same test was
792 performed for CD4⁺FOXP3⁻ and CD4⁺FOXP3⁺ cells.

793

794 The 10 LUAD patients with the highest adjacent-tumor lymphocytes to stromal cell ratio
795 were selected for this immune subset spatial projection. All samples had above median
796 CD8⁺%. One sample was excluded due to poor HE-IHC alignment quality and the
797 subsequent analysis was performed on the remaining nine samples. The quality of
798 alignment was evaluated by manually identifying 238 visible landmarks and placed on
799 corresponding positions in H&E and IHC tiles (total number of tiles = 249, maximum
800 landmarks per tile = 5), as shown in Extended Data Fig. 8b. These marked points were used
801 to compute the Euclidean distance (difference in x, y coordinates) between them to obtain a
802 quantitative measurement of alignment accuracy. The average distance between matching
803 landmarks was 9.57 μm , whereas the maximum distance between the H&E and
804 CD4/CD8/FOXP3 sections was 16 μm .

805

806 **Survival analysis and other statistical methods**

807 Survival tests were conducted using Kaplan-Meier estimator ('ggsurvplot' R function from
808 the 'survminer' and 'survival' R packages) as well as Cox model ('coxph' R function and
809 displayed using 'ggforest' R function). Forest plots show the hazard ratio in the x-axis; each
810 variable's hazard ratio is plotted and annotated with a 95% confidence interval. The
811 clinical parameters included in the multivariate model were age, sex, smoking pack years,
812 histology (whether LUAD, LUSC or otherwise), tumor stage, adjuvant therapy (whether

813 received or not). Because of its prognostic importance in TRACERx, the upper quartile of
814 clonal neoantigens in each histology cohort was also incorporated in the multivariate
815 model. The range of available disease-free survival data was 34-1364 days (median = 915
816 days) in TRACERx, and 1-6139 days (median = 684 days) in LATTICE-A. All hazard ratios
817 were computed on all time points (i.e. the whole survival curve, not at a specific time
818 point). Correlation tests used Spearman's method and were generated using the function
819 'ggscatter' from the 'ggpubr' R package. All correlation plots show the Rho (ρ) coefficient
820 and the significance R-value. For statistical comparisons among groups, a two-sided,
821 nonparametric, unpaired, Wilcoxon signed-rank test was used, unless stated otherwise. All
822 box plots were generated using the function 'ggboxplot' from the 'ggpubr' R package (all
823 data points are plotted with the 'jitter' option, the median value is indicated by a thick
824 horizontal line; minimum and maximum values are indicated by the extreme points; the
825 first and third quantiles are represented by the box edges; and vertical lines indicate the
826 error range) or the function 'ggbetweenstats' from the 'ggstatplot' R package for more
827 than two groups. Tests for concordance between two data classes were analyzed using a
828 Fisher's exact test. All statistical tests were two-sided, a R value of less than .05 was
829 considered statistically significant. To adjust R-values for multiple comparisons, the
830 Benjamini & Hochberg method was used. To measure effect size, Cohen's d method was
831 used. All statistical analyses were conducted in R (version 3.5.1).

832

833 **Reporting summary**

834 Further information on research design is available in the Nature Research Reporting
835 Summary linked to this paper.

836

837

838 **Extended Data Figures legends**

839

840 **Extended Data Fig. 1. CONSORT diagrams for TRACERx 100 and LATTICE-A histology**
841 **cohorts and patient characteristics.** **a.** TRACERx CONSORT diagram to illustrate sample
842 collection and analysis of regional and diagnostic histology samples, as well as the overlap
843 with RNA and DNA studies. **b.** TRACERx patient characteristics for the histology cohort. **c.**
844 LATTICE-A CONSORT diagram (= 970 LUAD patients). Legends for ‘type of the analysis’
845 correspond to panel **a.** **d.** Demographics and clinical patient characteristics for TRACERx
846 (top three panels) and LATTICE-A (bottom three panels) showing the distribution of age
847 (colored by sex), distribution of smoking pack years and the proportion of patients in each
848 pathological stage. Horizontal lines indicate the median value.

849

850 **Extended Data Fig. 2. Validation of the automated single-cell classification for H&E.** **a.** A
851 scatter plot showing the correlation between H&E-based adjacent-tumor
852 lymphocytes/stromal and pathology TIL estimates in diagnostic samples (= 98 diagnostic
853 slides/patients). **b.** Scatter plots showing the correlations between H&E-based tumor
854 cellularity estimate and ASCAT/VAF purity scores (= 238 regions; 83 patients). **c.** A scatter
855 plot showing the correlation between H&E-based estimate of lymphocyte percentage
856 among all cells and RNA-seq-based CD8⁺ signature using the Danaher et al. method³⁰ (=
857 142 regions; 56 patients). **d.** A scatter plot showing the correlation between H&E-based
858 estimate of lymphocyte percentage among all cells and CD8⁺ cell percentage in IHC in the
859 diagnostic samples (= 100 diagnostic slide/patients). **e.** Scatter plots showing the
860 correlation between H&E-based lymphocyte percentage versus pathological scores of
861 overall lymphocytic cell fraction, and adjacent-tumor lymphocytes/stromal versus
862 pathology TIL estimates in an external cohort (LATTICE-A, = 80 diagnostic slides/patients).
863 **f.** Illustrative example to show the spatial alignment of TTF1/CD45/SMA-stained IHC and
864 H&E images obtained using sequential staining on the same tissue microarray section for
865 biological validation. **g.** A scatter plot showing the correlation between stromal cell
866 percentage determined by H&E and SMA⁺ cell percentage per LUAD image tiles of size
867 100 μm^2 (= 144). The experiment was conducted once using one TMA (= 33
868 cores/patients). The shading indicates 95% confidence interval.

869

870 **Extended Data Fig. 3. Distribution of regional lymphocytic infiltration according to**
871 **pathological stage.** All available patients’ data have been used in this figure except for the
872 standard deviation tests excluding patients with a single tumor region. Patients without
873 pathological staging information from the LATTICE-A cohort were also removed. **a, b, c,**
874 top row: TRACERx and bottom row: LATTICE-A. Horizontal lines indicate the median value.

875 **a.** Distribution of the standard deviation of regional lymphocyte percentage for LUAD and
876 LUSC patients in TRACERx (= 69), and LUAD in LATTICe-A (= 814). **b.** Distribution of the
877 standard deviation of regional lymphocyte percentage across pathological stages (= 69 for
878 TRACERx, 814 for LATTICe-A). **c.** Distribution of regional mean of lymphocyte percentage
879 across stages (= 79 for TRACERx, 827 for LATTICe-A). **d.** No significant difference among
880 stages with respect to standard deviation (= 69 for TRACERx, 814 for LATTICe-A) or mean (=
881 = 79 for TRACERx, 827 for LATTICe-A) of regional lymphocytic infiltration. Left panel,
882 TRACERx and right panel, LATTICe-A. Correction for multiple testing was applied in **d**, for
883 each cohort individually. A two-sided, non-parametric, unpaired, Wilcoxon signed-rank
884 test was used; each dot represents a patient; the mean value is annotated with a large
885 dot; the median value is represented by a thick horizontal line; minimum and maximum
886 values are indicated by the extreme points; the first and third quantiles are represented by
887 the box edges; and the violin shape shows the data distribution as a kernel density
888 estimation.

889

890 **Extended Data Fig. 4. Validation of immune phenotype classification.** **a.** The proposed
891 immune classification imposed on density plot showing distribution of lymphocyte
892 percentage. The middle zone corresponds to the intermediate phenotype, red zone for
893 immune hot and blue zone for immune cold. Black dash line shows the median. This
894 classification was validated after applying small perturbations to the thresholds to re-
895 classify regional immune phenotypes, illustrated as grey dash lines: no intermediate zone
896 (i.e. hard median for separating hot and cold), standard deviation (SD)/2 above and below
897 the median, SD/3 and SD/6. **b.** Forest plots to show repeated multivariate Cox regression
898 tests for the number of immune cold regions using these new classifications (= 79
899 patients), after accounting for stage, total number of samples, upper quartile of clonal
900 neoantigens determined for LUAD and LUSC individually, and other clinical parameters.
901 Box plots showing difference in genomic distance for pairs of hot regions compared with
902 pairs of cold regions for LUAD and LUSC separately (LUAD: = 45 hot pairs, 45 cold pairs for
903 no intermediate zone; = 19 hot, 25 cold for SD/2; = 25 hot, 33 cold for SD/3; = 32 hot, 41
904 cold for SD/6. LUSC: = 32 hot pairs, 54 cold pairs for no intermediate zone; = 19 hot, 27
905 cold for SD/2; = 19 hot, 37 cold for SD/3; = 27 hot, 41 cold for SD/6.). **c.** Box plots showing
906 significant difference in CD8⁺ RNA-seq signature using the Danaher method between
907 regions of hot and cold phenotype across all classification schemes (= 219 for SD/4; 275
908 for no intermediate zone; 173 for SD/2; 204 for SD/3; 237 for SD/6). **d.** Distribution and
909 difference of lymphocytic infiltration for LUAD versus LUSC regions in TRACERx (= 275
910 regions; 85 patients) as well as distribution for LUAD in LATTICe-A (= 4,324 samples; 970
911 patients). Horizontal lines in the distribution plots indicate mean values. For statistical
912 comparisons among groups, a two-sided, non-parametric, unpaired, Wilcoxon signed-rank
913 test was used, unless stated otherwise.

914

915 **Extended Data Fig. 5. Concordance between histology deep learning and RNA-seq**
916 **immune classification.** **a.** A box plot showing the difference in pathology TIL estimates
917 between immune hot and immune cold regions (= 219). Pathology TIL estimates score
918 fraction of stroma containing TILs, whereas immune classification was defined based on
919 the percentage of lymphocytes in all cells within a slide. **b.** A confusion matrix to compare
920 RNA-seq and deep learning histology immune classifications (discarding immune
921 intermediate regions, = 109 regions (57 LUAD, 37 LUSC, 15 other histology subtypes); 52
922 patients). The p-value was generated using a two-sided Fisher's exact test for overlap. **c.** A
923 box plot showing the difference in the fraction of immune hotspots³⁶ in regions where the
924 two classifications are in agreement (= 78; labeled as 'In agreement') against the
925 discrepant regions (= 31, labeled as 'Discrepant'). Each dot represents a region, the
926 median value is indicated by a thick horizontal line; minimum and maximum values are
927 indicated by the extreme points; and the first and third quantiles are represented by the
928 box edges. **d.** Box plots to support the overall consistency between H&E-deep learning and
929 RNA-seq methods by comparing different immune scores as well as ASCAT tumor purity
930 between immune hot/high and cold/low tumor regions (all R -values < 0.0001). Top row,
931 H&E-deep learning immune classification (= 219; except the ASCAT purity box plot = 186
932 regions), bottom row, RNAseq derived immune classification (= 142; except the ASCAT
933 purity box plot, = 141 regions). For statistical comparisons among groups, a two-sided,
934 non-parametric, unpaired, Wilcoxon signed-rank test was used, unless stated otherwise.

935

936 **Extended Data Fig. 6. Genomic and survival analysis of tumor regions according to**
937 **immune phenotypes.** **a.** A box plot showing the difference in genomic distances for pairs
938 of immune hot versus immune cold regions within the same LUSC patients (= 59 pairs). A
939 two-sided, non-parametric, unpaired, Wilcoxon signed-rank test was used. **b.** Forest plots
940 to show the univariate prognostic value for the number of immune low regions (both as
941 continuous and dichotomized at the median (≤ 1 versus > 1)), or the number of immune
942 high regions, using the immune classification generated by RNA-seq-based infiltrating
943 immune cell populations¹ in 64 TRACERx tumors (41 LUAD, 16 LUSC and 7 other histology
944 subtypes).
945 **c.** Forest plots showing multivariate Cox regression analyses in both TRACERx (= 79
946 patients; LUAD and LUSC combined) and LATTICe-A (= 651 LUAD patients representing a
947 subset with complete stage and smoking pack years data) with the number of immune
948 cold regions dichotomized at the median (≤ 1 versus > 1). This remains significant when the
949 number of immune cold regions was replaced as a continuous variable, in the same
950 multivariate model, (R = 0.019 in TRACERx and < 0.001 in LATTICe-A, for the number of
951 immune cold regions). Clonal neoantigens were dichotomized using the upper quartile,

952 determined individually for LUAD and LUSC tumors¹. **d.** The same test in **c** when tumor size
953 (in mm) was also controlled in the multivariate model in LATTICE-A. This test also
954 remained significant for a bigger group of patients with complete stage data, but missing
955 pack years information (= 815, $R < 0.001$, $HR = 1.4[1.1-1.8]$). **e.** Forest plots to compare
956 the prognostic value of regional immune scores as well as diagnostic H&E and IHC scores
957 for relapse-free survival in TRACERx (= 79 patients, LUAD and LUSC combined). Wherever
958 possible, these immune features were tested in LATTICE-A (= 970 patients). To compare
959 the prognostic value of the number of immune cold region with other immune features,
960 LATTICE-A comparisons were conducted in Cox multivariate regression models to include
961 every immune feature after correcting for the number of immune cold regions in the same
962 model. Each variable's HR is plotted with a 95% confidence interval; all R-values were
963 adjusted for multiple testing; and the size of the circles denotes $-\log_{10}(P)$. For the
964 sake of visualization, a minor adjustment was made to the HR for the number of cold
965 regions/total number of regions in LATTICE-A from 0.88[0.57-1.3] to 0.99[0.97-1.3]. SD:
966 standard deviation, used for measuring variability of lymphocyte percentage among
967 samples within a tumor. **f.** Forest plots using Cox multivariate regression analysis showing
968 that the prognostic value of the number of immune cold regions was independent of: 1)
969 genetic measure, subclonal copy number alteration (obtained from ⁶); 2) tumor cellularity
970 from DNA-seq-based ASCAT purity, 3) tumor cellularity measured by deep learning-based
971 cancer cell percentage. **g.** Kaplan Meier curves to illustrate the difference in relapse-free
972 survival for TRACERx patients including other histology types (= 85; representing all
973 TRACERx patients in the multiregion histology cohort) with high and low number of
974 immune cold regions, dichotomized by its median value. Log-rank $R = 0.0017$. **h.** Forest
975 plot using Cox regression for the multivariate survival analysis for the number of immune
976 cold regions in TRACERx including patients with other histology subtypes (= 85).

977

978 **Extended Data Fig. 7. Fractal dimension and relationships with stromal cells.** **a.**
979 Distribution of the average minimum Euclidean distance between a stromal cell to its
980 neighboring cancer cell. For every stromal cell in a tumor region slide, the minimum
981 distance to nearest cancer cell was computed. This distance was then averaged for all
982 identified stromal cells in every region to plot the distribution (= 275 regions; 85 patients).
983 **b.** Distribution of the fractal dimension of the cancer-stroma cell interface for histology
984 types in the TRACERx cohort (= 275 regions; 85 patients). **c.** Box plots to show the
985 difference in fractal dimension between immune hot and cold regions in TRACERx LUAD (=
986 113) and LUSC (= 84). **d.** Box plots showing the difference in stromal cell percentage
987 between immune hot and cold regions in all (= 219), LUAD (= 113), and LUSC (= 84). **e.**
988 Scatter plots showing the correlation between fractal dimension and percentage of cells
989 that are stromal or cancer in all tumor regions (= 275 regions; 85 patients). This shows
990 that fractal dimension was independent of tumor cell composition, with only a weak

991 correlation with stromal cell percentage and no correlation with tumor cellularity. **f.** Box
992 plots showing the difference in fractal dimension between LUAD tumor regions harboring
993 an LOH event for HLA type A (= 106), type B (= 113), type C (= 108) versus regions that do
994 not, adjusted for multiple comparisons with the corresponding test in Fig. 4c. **g.** The same
995 test in **f** repeated for LUSC tumor regions (= 87) for HLA of any type. **h.** Box plots showing
996 the difference in tumor-level fractal dimension using the maximum value of regional
997 measures between LUAD tumors (= 48) harboring a single LOH event for any HLA type,
998 HLA type A, type B and type C versus tumors that do not, independent of predicted clonal
999 neoantigens. Each p-value was generated using a multiple regression linear model and was
1000 also adjusted for multiple testing correction. **i.** The same test in **h** repeated for LUSC
1001 tumors (= 29) for HLA of any type. For statistical comparisons among groups, a two-sided,
1002 non-parametric, unpaired, Wilcoxon signed-rank test was used, unless stated otherwise.

1003

1004 **Extended Data Fig. 8. Relationship of immune subsets and spatial TILs in LUAD. a.**
1005 Spearman's correlations between immune scores in diagnostic slides and genetic
1006 measures including predicted neoantigens and HLALOH in LUAD patients (= 46). ICLR:
1007 intra-tumor lymphocytes to total tumor cell ratio. Only significant correlations after
1008 multiple testing are highlighted ($\rho = 0.37$, $R = 0.035$). **b.** Examples of registered H&E and
1009 IHC tiles. The green cross denotes a manually placed landmark repeated 238 times on
1010 pairs of H&E-IHC image tiles. The Euclidean distance (difference in , coordinates) was
1011 computed between the two landmarks which was then **c.** shown as a distribution to
1012 represent the accuracy of the registration (= 249 total H&E-IHC image tiles, maximum five
1013 landmarks per a pair of tiles). The average distance between matching landmarks was
1014 $9.57\mu\text{m}$ and the distribution is within the expected range of maximum distance between
1015 four serial sections ($16\mu\text{m}$). **d.** Box plots to illustrate the difference in percentage of
1016 immune cell subsets among adjacent, intra and distal-tumor lymphocytes (= 20 image
1017 tiles), a non-parametric, paired Wilcoxon test was used.

1018

1019 **Extended Data Fig. 9. Summary of immune and genomics features in NSCLC.** An extended
1020 heatmap showing all immune variables described in TRACERx across all patients (= 275
1021 regions; 85 patients), along with genetic measures and clinical parameters. Each column
1022 represents a tumor, grouped by their histologic subtype. Tumor regions (illustrated as
1023 dots) were assigned to immune hot, immune cold and intermediate phenotypes based on
1024 percentage of lymphocytes in all cells following H&E-based deep learning analysis.
1025 Cancerstromal fractal dimension, defined using the maximum fractal dimension in regions
1026 of a patient, using the median as cut-off to determine high and low groups.

1027

1028 **Methods and Extended Data References**

1029

1030 27. Raza, S. E. A. et al. Micro-Net: A unified model for segmentation of various objects
1031 in microscopy images. *Med. Image Anal.* 52, 160–173 (2019).

1032 28. Sirinukunwattana, K. et al. Locality Sensitive Deep Learning for Detection and
1033 Classification of Nuclei in Routine Colon Cancer Histology Images. *IEEE Trans. Med.*
1034 *Imaging* 35, 1196–1206 (2016).

1035 29. Abadi, M. et al. TensorFlow: Large-Scale Machine Learning on Heterogeneous
1036 Distributed Systems. (2016).

1037 30. Danaher, P. et al. Gene expression markers of Tumor Infiltrating Leukocytes. *J.*
1038 *Immunother. Cancer* 5, 18 (2017).

1039 31. HOLZINGER, A. et al. Monoclonal Antibody to Thyroid Transcription Factor-1:
1040 Production, Characterization, and Usefulness in Tumor Diagnosis. *Hybridoma* 15, 49–53
1041 (1996).

1042 32. Matoso, A. et al. Comparison of thyroid transcription factor-1 expression by 2
1043 monoclonal antibodies in pulmonary and nonpulmonary primary tumors. *Appl.*
1044 *Immunohistochem. Mol. Morphol. AIMM* 18, 142–9 (2010).

1045 33. Pelosi, G. et al. Δ Np63 (p40) and Thyroid Transcription Factor-1 Immunoreactivity
1046 on Small Biopsies or Cellblocks for Typing Non-small Cell Lung Cancer: A Novel Two-Hit,
1047 Sparing-Material Approach. *J. Thorac. Oncol.* 7, 281–290 (2012).

1048 34. Heindl, A. et al. Relevance of Spatial Heterogeneity of Immune Infiltration for
1049 Predicting Risk of Recurrence After Endocrine Therapy of ER+ Breast Cancer. *JNCI J. Natl.*
1050 *Cancer Inst.* 110, (2018).

1051 35. Heindl, A. et al. Microenvironmental niche divergence shapes BRCA1-dysregulated
1052 ovarian cancer morphological plasticity. *Nat. Commun.* 9, 3917 (2018).

1053 36. Nawaz, S., Heindl, A., Koelble, K. & Yuan, Y. Beyond immune density: critical role of
1054 spatial heterogeneity in estrogen receptor-negative breast cancer. *Mod. Pathol.* 28, 766–
1055 777 (2015).

1056 37. Dubuc, Quiniou, Roques-Carmes, Tricot & Zucker. Evaluating the fractal dimension
1057 of profiles. *Phys. Rev. A, Gen. Phys.* 39, 1500–1512 (1989).

1058 38. MOISY, F. & JIMÉNEZ, J. Geometry and clustering of intense structures in isotropic
1059 turbulence. *J. Fluid Mech.* 513, 111–133 (2004).

1060 39. Francis, K. & Palsson, B. O. Effective intercellular communication distances are
1061 determined by the relative time constants for cyto/chemokine secretion and diffusion.
1062 *Proc. Natl. Acad. Sci. U. S. A.* 94, 12258–62 (1997).

1063

1044

1045

1045 **References**

1046

- 1047 1. Rosenthal, R. *et al.* Neoantigen-directed immune escape in lung cancer evolution.
1048 *Nature* **1** (2019). doi:10.1038/s41586-019-1032-7
- 1049 2. Morris, L. G. T. & Chan, T. A. Lung Cancer Evolution: What's Immunity Got to Do
1050 with It? *Cancer Cell* **35**, 711–713 (2019).
- 1051 3. Morris, L. G. T. *et al.* Pan-cancer analysis of intratumor heterogeneity as a
1052 prognostic determinant of survival. *Oncotarget* **7**, 10051–10063 (2016).
- 1053 4. Milo, I. *et al.* The immune system profoundly restricts intratumor genetic
1054 heterogeneity. *Sci. Immunol.* **3**, (2018).
- 1055 5. Jia, Q. *et al.* Local mutational diversity drives intratumoral immune heterogeneity in
1056 non-small cell lung cancer. *Nat. Commun.* **9**, (2018).
- 1057 6. Jamal-Hanjani, M. *et al.* Tracking the Evolution of Non-Small-Cell Lung Cancer. *N.*
1058 *Engl. J. Med.* **376**, 2109–2121 (2017).
- 1059 7. Hendry, S. *et al.* Assessing Tumor-Infiltrating Lymphocytes in Solid Tumors. *Adv.*
1060 *Anat. Pathol.* **24**, 311–335 (2017).
- 1061 8. Moore, D. A. *et al.* In situ growth in early lung adenocarcinoma may represent
1062 precursor growth or invasive clone outgrowth—a clinically relevant distinction.
1063 *Mod. Pathol.* **1** (2019). doi:10.1038/s41379-019-0257-1
- 1064 9. Whittaker, K. A. & Ryneerson, T. A. Evidence for environmental and ecological
1065 selection in a microbe with no geographic limits to gene flow. *Proc. Natl. Acad. Sci.*
1066 *U. S. A.* **114**, 2651–2656 (2017).
- 1067 10. Shafer, A. B. A. & Wolf, J. B. W. Widespread evidence for incipient ecological
1068 speciation: A meta-analysis of isolation-by-ecology. *Ecology Letters* **16**, 940–950
1069 (2013).
- 1070 11. Costa, A. *et al.* Fibroblast Heterogeneity and Immunosuppressive Environment in
1071 Human Breast Cancer. *Cancer Cell* **33**, 463–479.e10 (2018).
- 1072 12. Öhlund, D. *et al.* Distinct populations of inflammatory fibroblasts and
1073 myofibroblasts in pancreatic cancer. *J. Exp. Med.* **214**, 579–596 (2017).
- 1074 13. Salmon, H. *et al.* Matrix architecture defines the preferential localization and
1075 migration of T cells into the stroma of human lung tumors. *J. Clin. Invest.* **122**, 899–
1076 910 (2012).
- 1077 14. Thomas, D. A. & Massagué, J. TGF- β directly targets cytotoxic T cell functions during
1078 tumor evasion of immune surveillance. *Cancer Cell* **8**, 369–380 (2005).
- 1079 15. Joyce, J. A. & Fearon, D. T. T cell exclusion, immune privilege, and the tumor
1080 microenvironment. *Science (80-.)*. **348**, 74–80 (2015).
- 1081 16. Sorokin, L. The impact of the extracellular matrix on inflammation. *Nat. Rev.*
1082 *Immunol.* **10**, 712–723 (2010).
- 1083 17. Chen, D. S. & Mellman, I. Elements of cancer immunity and the cancer-immune set
1084 point. *Nature* **541**, 321–330 (2017).

- 1085 18. McGranahan, N. *et al.* Allele-Specific HLA Loss and Immune Escape in Lung Cancer
1086 Evolution. *Cell* **171**, 1259-1271.e11 (2017).
- 1087 19. McGranahan, N. *et al.* Clonal neoantigens elicit T cell immunoreactivity and
1088 sensitivity to immune checkpoint blockade. *Science (80-.)*. **351**, (2016).
- 1089 20. Yuan, Y. Modelling the spatial heterogeneity and molecular correlates of
1090 lymphocytic infiltration in triple-negative breast cancer. *J. R. Soc. Interface* **12**,
1091 20141153 (2015).
- 1092 21. Thomas, A., Liu, S. V., Subramaniam, D. S. & Giaccone, G. Refining the treatment of
1093 NSCLC according to histological and molecular subtypes. *Nat. Rev. Clin. Oncol.* **12**,
1094 511–526 (2015).
- 1095 22. Hammerman, P. S. *et al.* Comprehensive genomic characterization of squamous cell
1096 lung cancers. *Nature* **489**, 519–525 (2012).
- 1097 23. Collisson, E. A. *et al.* Comprehensive molecular profiling of lung adenocarcinoma:
1098 The cancer genome atlas research network. *Nature* **511**, 543–550 (2014).
- 1099 24. Keren, L. *et al.* A Structured Tumor-Immune Microenvironment in Triple Negative
1100 Breast Cancer Revealed by Multiplexed Ion Beam Imaging. *Cell* **174**, 1373-1387.e19
1101 (2018).
- 1102 25. Giesen, C. *et al.* Highly multiplexed imaging of tumor tissues with subcellular
1103 resolution by mass cytometry. *Nat. Methods* **11**, 417–422 (2014).
- 1104 26. Goltsev, Y. *et al.* Deep Profiling of Mouse Splenic Architecture with CODEX
1105 Multiplexed Imaging. *Cell* **174**, 968-981.e15 (2018).
- 1106 27. Raza, S. E. A. *et al.* Micro-Net: A unified model for segmentation of various objects
1107 in microscopy images. *Med. Image Anal.* **52**, 160–173 (2019).
- 1108 28. Sirinukunwattana, K. *et al.* Locality Sensitive Deep Learning for Detection and
1109 Classification of Nuclei in Routine Colon Cancer Histology Images. *IEEE Trans. Med.*
1110 *Imaging* **35**, 1196–1206 (2016).
- 1111 29. Abadi, M. *et al.* TensorFlow: Large-Scale Machine Learning on Heterogeneous
1112 Distributed Systems. (2016).
- 1113 30. Danaher, P. *et al.* Gene expression markers of Tumor Infiltrating Leukocytes. *J.*
1114 *Immunother. Cancer* **5**, 18 (2017).
- 1115 31. HOLZINGER, A. *et al.* Monoclonal Antibody to Thyroid Transcription Factor-1:
1116 Production, Characterization, and Usefulness in Tumor Diagnosis. *Hybridoma* **15**,
1117 49– 53 (1996).
- 1118 32. Matoso, A. *et al.* Comparison of thyroid transcription factor-1 expression by 2
1119 monoclonal antibodies in pulmonary and nonpulmonary primary tumors. *Appl.*
1120 *Immunohistochem. Mol. Morphol. AIMM* **18**, 142–9 (2010).
- 1121 33. Pelosi, G. *et al.* ΔNp63 (p40) and Thyroid Transcription Factor-1 Immunoreactivity
1122 on Small Biopsies or Cellblocks for Typing Non-small Cell Lung Cancer: A Novel Two-
1123 Hit, Sparing-Material Approach. *J. Thorac. Oncol.* **7**, 281–290 (2012).

- 1124 34. Heindl, A. *et al.* Relevance of Spatial Heterogeneity of Immune Infiltration for
1125 Predicting Risk of Recurrence After Endocrine Therapy of ER+ Breast Cancer. *JNCI J.*
1126 *Natl. Cancer Inst.* **110**, (2018).
- 1127 35. Heindl, A. *et al.* Microenvironmental niche divergence shapes BRCA1-dysregulated
1128 ovarian cancer morphological plasticity. *Nat. Commun.* **9**, 3917 (2018).
- 1129 36. Nawaz, S., Heindl, A., Koelble, K. & Yuan, Y. Beyond immune density: critical role of
1130 spatial heterogeneity in estrogen receptor-negative breast cancer. *Mod. Pathol.* **28**,
1131 766–777 (2015).
- 1132 37. Dubuc, Quiniou, Roques-Carmes, Tricot & Zucker. Evaluating the fractal dimension
1133 of profiles. *Phys. Rev. A, Gen. Phys.* **39**, 1500–1512 (1989).
- 1134 38. MOISY, F. & JIMÉNEZ, J. Geometry and clustering of intense structures in isotropic
1135 turbulence. *J. Fluid Mech.* **513**, 111–133 (2004).
- 1136 39. Francis, K. & Palsson, B. O. Effective intercellular communication distances are
1137 determined by the relative time constants for cyto/chemokine secretion and
1138 diffusion. *Proc. Natl. Acad. Sci. U. S. A.* **94**, 12258–62 (1997).

1139 **Geospatial immune variability illuminates differential evolution of lung**
1140 **adenocarcinoma**

1141

1142

1143 **TRACERx consortium member names**

1144 Charles Swanton (3,4,5), Mariam Jamal-Hanjani (3,5), John Le Quesne (10,11,15), Allan
1145 Hackshaw (12), Sergio A Quezada (13), Nicholas McGranahan (3,14), Rachel Rosenthal
1146 (3,4), Crispin T Hiley (3,4), Selvaraju Veeriah (3,4), David A Moore (3,6), Maise Al Bakir (4),
1147 Teresa Marafioti (6), Roberto Salgado (8,9), Yenting Ngai (12), Abigail Sharp (12), Cristina
1148 Rodrigues

1149 (12), Oliver Pressey (12), Sean Smith (12), Nicole Gower (12), Harjot Dhanda (12), Joan
1150 Riley (16), Lindsay Primrose (16), Luke Martinson (16), Nicolas Carey (16), Jacqui A Shaw
1151 (16), Dean Fennell (16,28), Gareth A Wilson (17), Nicolai J Birckbak (17), Thomas B K
1152 Watkins (17), Mickael Escudero (17), Aengus Stewart (17), Andrew Rowan (17), Jacki
1153 Goldman (17), Peter Van Loo (17), Richard Kevin Stone (17), Tamara Denner (17), Emma
1154 Nye (17), Sophia Ward (17), Emilia L Lim (17), Stefan Boeing (17), Maria Greco (17), Kevin
1155 Litchfield (17), Jerome Nicod (17), Clare Puttick (17), Katey Enfield (17), Emma Colliver (17),
1156 Brittany Campbell (17), Christopher Abbosh (18), Yin Wu (18), Marcin Skrzypski (18),
1157 Robert E Hynds (18), Andrew Georgiou (18), Mariana Werner Sunderland (18), James L
1158 Reading (18), Karl S Peggs (18), John A Hartley (18), Pat Gorman (18), Helen L Lowe (18),
1159 Leah Ensell (18), Victoria Spanswick (18), Angeliki Karamani (18), Dhruva Biswas (18),
1160 Maryam Razaq (18), Stephan Beck (18), Ariana Huebner (18), Michelle Dietzen (18),
1161 Cristina Naceur-Lombardelli (18), Mita Afroza Akther (18), Haoran Zhai (18), Nnennaya
1162 Kannu (18), Elizabeth Manzano (18), Supreet Kaur Bola (18), Ehsan Ghorani (18), Marc
1163 Robert de Massy (18), Elena Hoxha (18), Emine

1164 Hatipoglu (18), Stephanie Ogwuru (18), Benny Chain (18), Gillian Price (19), Sylvie
1165 DuboisMarshall (19), Keith Kerr (19), Shirley Palmer (19), Heather Cheyne (19), Joy Miller
1166 (19), Keith Buchan (19), Mahendran Chetty (19), Mohammed Khalil (19), Veni Ezhil (20),
1167 Vineet Prakash (20), Girija Anand (21), Sajid Khan (21), Kelvin Lau (22), Michael Sheaff (22),
1168 Peter Schmid (22), Louise Lim (22), John Conibear (22), Roland Schwarz (23,24,25),
1169 Jonathan Tugwood (26), Jackie Pierce (26), Caroline Dive (26,27), Ged Brady (26,27),
1170 Dominic G Rothwell (26,27), Francesca Chemi (26,27), Elaine Kilgour (26,27), Fiona
1171 Blackhall (27,30), Lynsey Priest (27,30), Matthew G Krebs (27,30), Philip Crosbie (27,51,52),
1172 Apostolos Nakas (28), Sridhar Rathinam (28), Louise Nelson (28), Kim Ryanna (28),
1173 Mohamad Tuffail (28), Amrita Bajaj (28), Jan Brozik (28), Fiona Morgan (29), Malgorzata
1174 Kornaszewska (29), Richard Attanoos (29), Haydn Adams (29), Helen Davies (29), Mathew
1175 Carter (30), Lindsay CR (30), Fabio Gomes (30), Zoltan Szallasi (31), Istvan Csabai (32),
1176 Miklos Diossy (32), Hugo Aerts (33,34), Alan Kirk (35), Mo Asif (35), John Butler (35), Rocco
1177 Bilanca (35), Nikos Kostoulas (35), Mairead MacKenzie (36), Maggie Wilcox (36), Sara

1178 Busacca (37), Alan Dawson (37), Mark R Lovett (37), Michael Shackcloth (38), Sarah Feeney
1179 (38), Julius Asante-Siaw (38), John Gosney (39), Angela Leek (40), Nicola Totten (40), Jack
1180 Davies Hodgkinson (40), Rachael Waddington (40), Jane Rogan (40), Katrina Moore (40),
1181 William Monteiro (41), Hilary Marshall (41), Kevin G Blyth (42), Craig Dick (42), Andrew
1182 Kidd (42), Eric Lim (43), Paulo De Sousa (43), Simon Jordan (43), Alexandra Rice (43),
1183 Hilgardt Raubenheimer (43), Harshil Bhayani (43), Morag Hamilton (43), Lyn Ambrose (43),
1184 Anand Devaraj (43), Hema Chavan (43), Sofina Begum (43), Aleksander Mani (43), Daniel
1185 Kaniu (43), Mpho Malima (43), Sarah Booth (43), Andrew G Nicholson (43), Nadia
1186 Fernandes (43), Jessica E Wallen (43), Pratibha Shah (43), Sarah Danson (44), Jonathan
1187 Bury (44), John Edwards (44), Jennifer Hill (44), Sue Matthews (44), Yota Kitsanta (44),
1188 Jagan Rao (44), Sara Tenconi (44), Laura Socci (44), Kim Suvarna (44), Faith Kibutu (44),
1189 Patricia Fisher (44), Robin Young (44), Joann Barker (44),
1190 Fiona Taylor (44), Kirsty Lloyd (44), Teresa Light (45), Tracey Horey (45), Dionysis
1191 PapadatosPastos (45, 47), Peter Russell (45), Sara Lock (46), Kayleigh Gilbert (46), David
1192 Lawrence (47), Martin Hayward (47), Nikolaos Panagiotopoulos (47), Robert George (47),
1193 Davide Patrini
1194 (47), Mary Falzon (47), Elaine Borg (47), Reena Khiroya (47), Asia Ahmed (47), Magali
1195 Taylor (47), Junaid Choudhary (47), Penny Shaw (47), Sam M Janes (47), Martin Forster
1196 (47), Tanya Ahmad (47), Siow Ming Lee (47), Javier Herrero (47), Dawn Carnell (47),
1197 Ruheena Mendes (47), Jeremy George (47), Neal Navani (47), Marco Scarci (47), Elisa
1198 Bertoja (47), Robert CM Stephens (47), Emilie Martinoni Hoogenboom (47), James W
1199 Holding (47), Steve Bandula (47), Babu Naidu (48), Gerald Langman (48), Andrew Robinson
1200 (48), Hollie Bancroft (48), Amy Kerr (48), Salma Kadiri (48), Charlotte Ferris (48), Gary
1201 Middleton (48), Madava Djearaman (48), Akshay Patel (48), Christian Ottensmeier (49),
1202 Serena Chee (49), Benjamin Johnson (49), Aiman Alzetani (49), Emily Shaw (49), Jason
1203 Lester (50), Yvonne Summers (51), Raffaele Califano (51), Paul Taylor (51), Rajesh Shah
1204 (51), Piotr Krysiak (51), Kendadai Rammohan (51), Eustace Fontaine (51), Richard Booton
1205 (51), Matthew Evison (51), Stuart Moss (51), Juliette Novasio (51), Leena Joseph (51), Paul
1206 Bishop (51), Anshuman Chaturvedi
1207 (51), Helen Doran (51), Felice Granato (51), Vijay Joshi (51), Elaine Smith (51), Angeles
1208 Montero (51)

1209

1210 **TRACERx consortium affiliations**

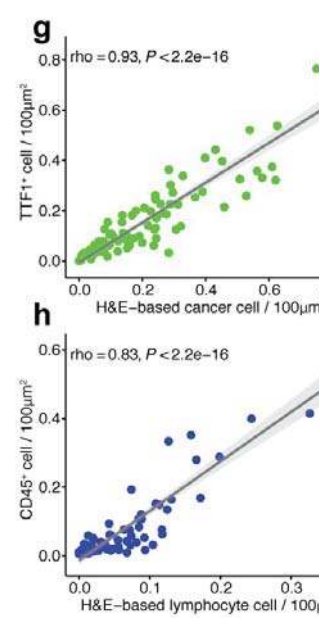
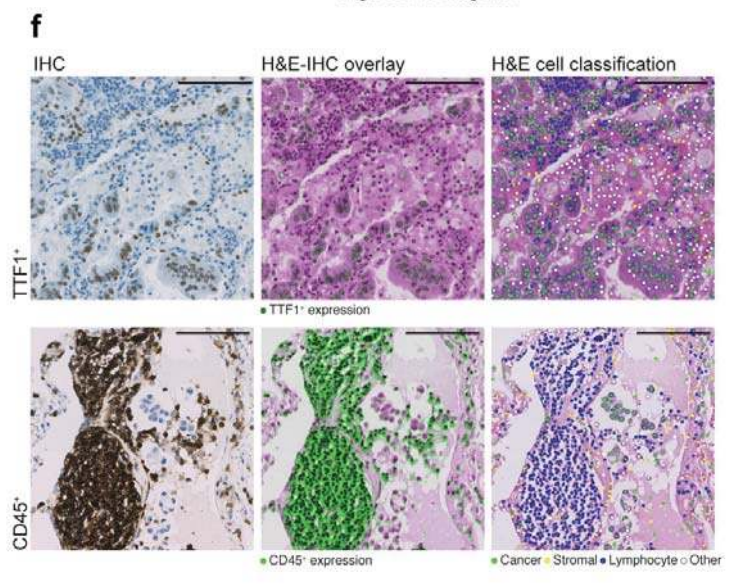
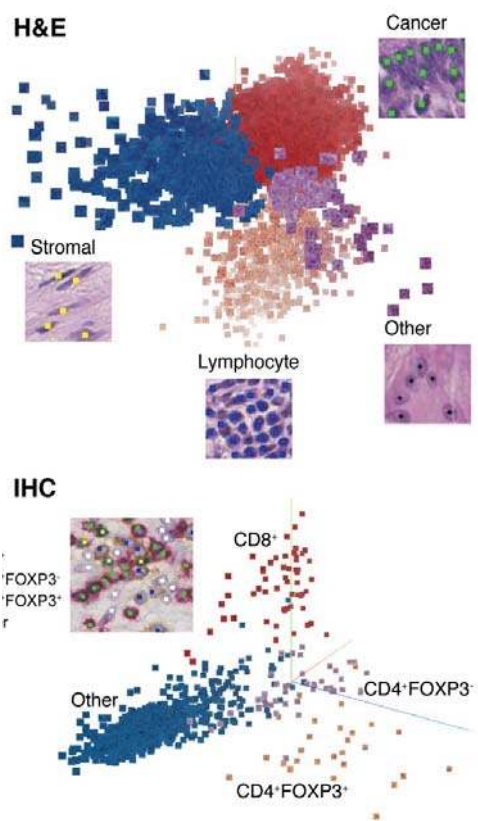
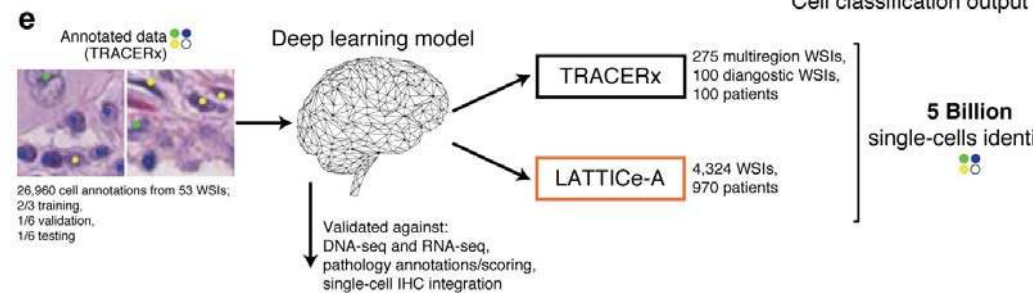
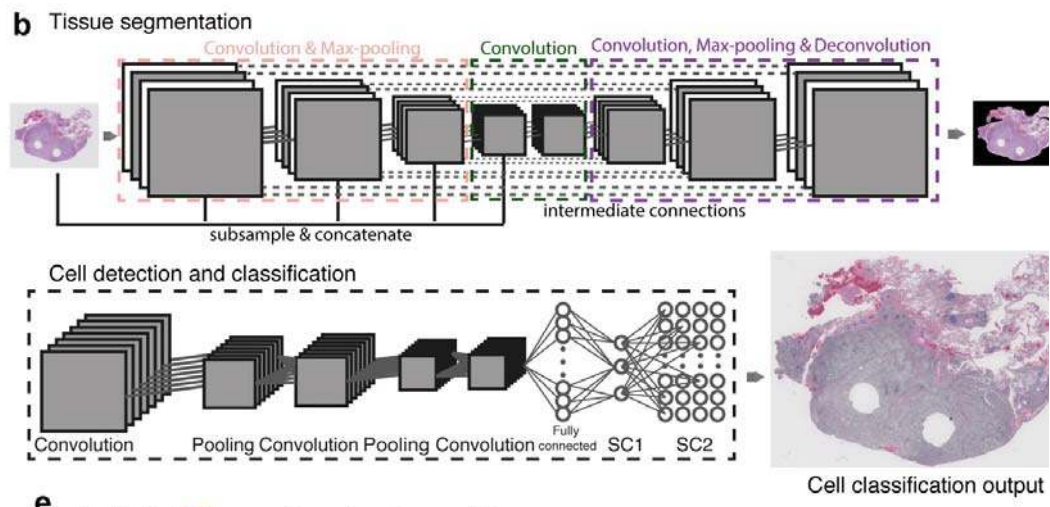
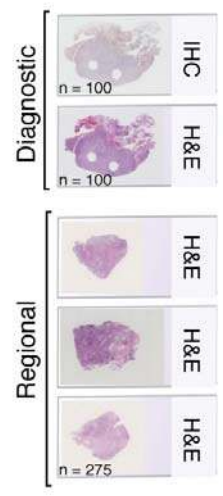
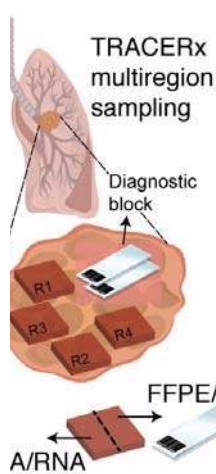
1211 (3) Cancer Research UK Lung Cancer Centre of Excellence, University College London Cancer
1212 Institute, London, UK

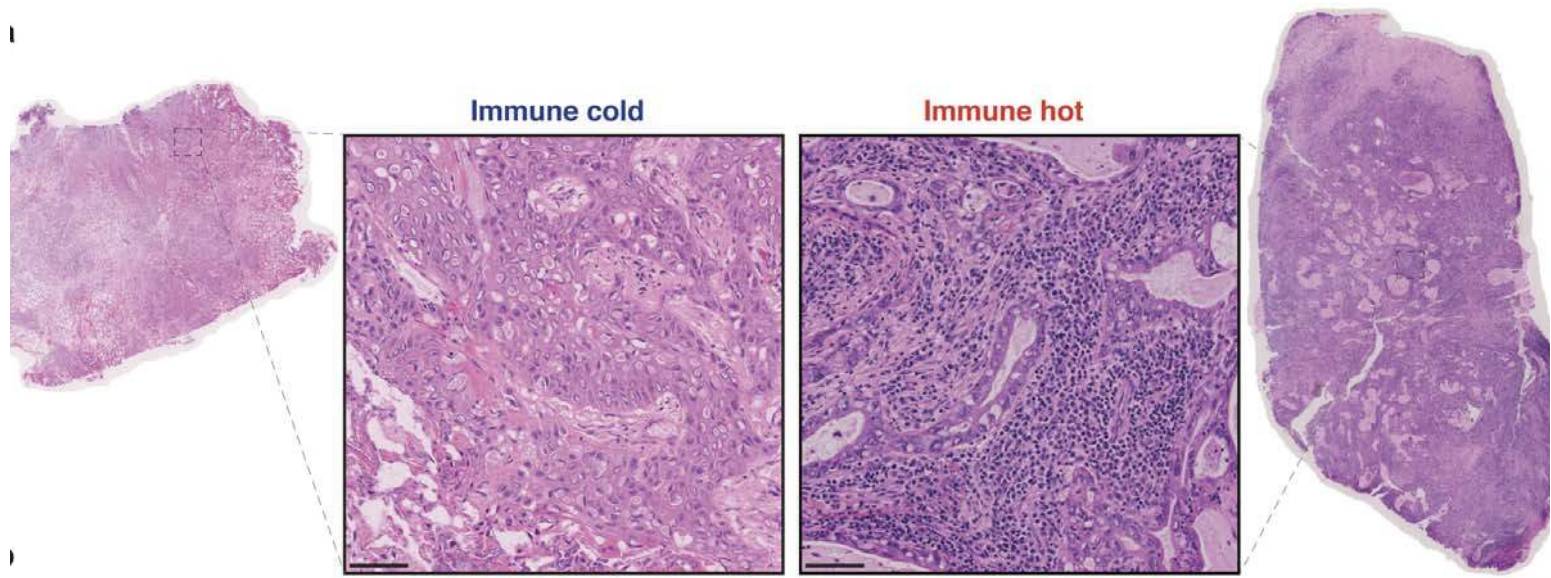
1213 (4) Cancer Evolution and Genome Instability Laboratory, The Francis Crick Institute, London,
1214 UK

1215 (5) Department of Medical Oncology, University College London Hospitals NHS Foundation
1216 Trust, London, UK

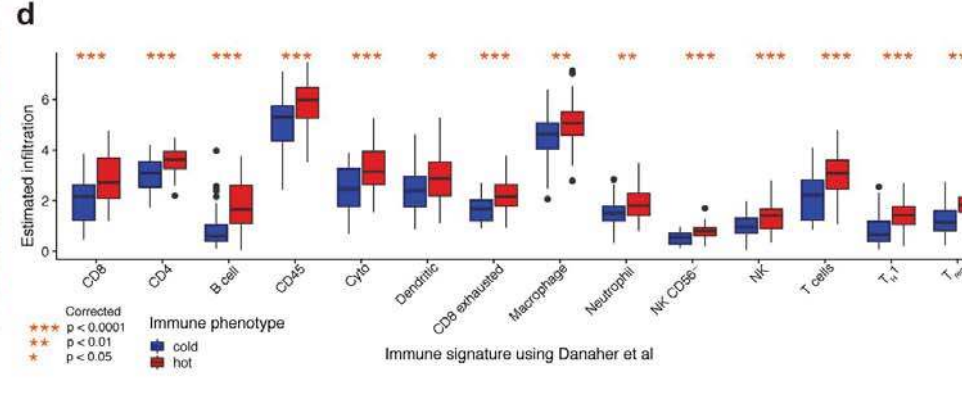
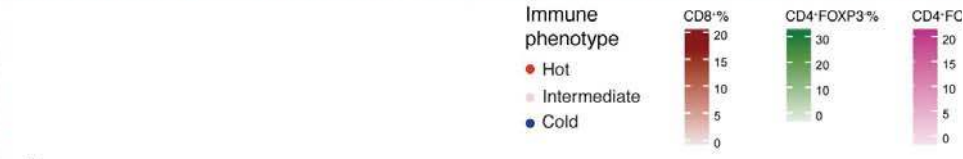
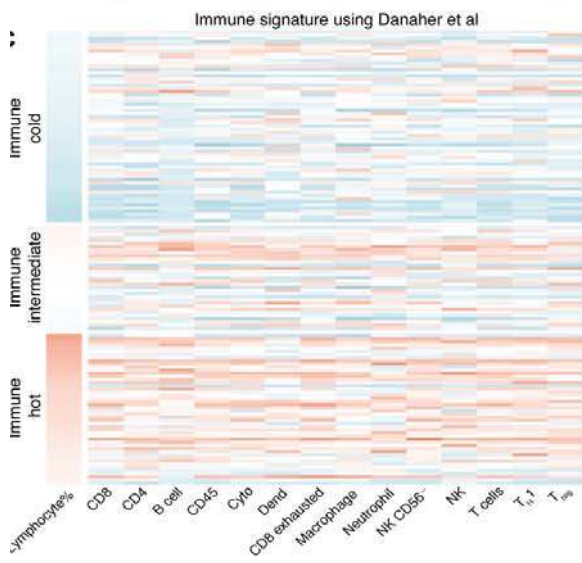
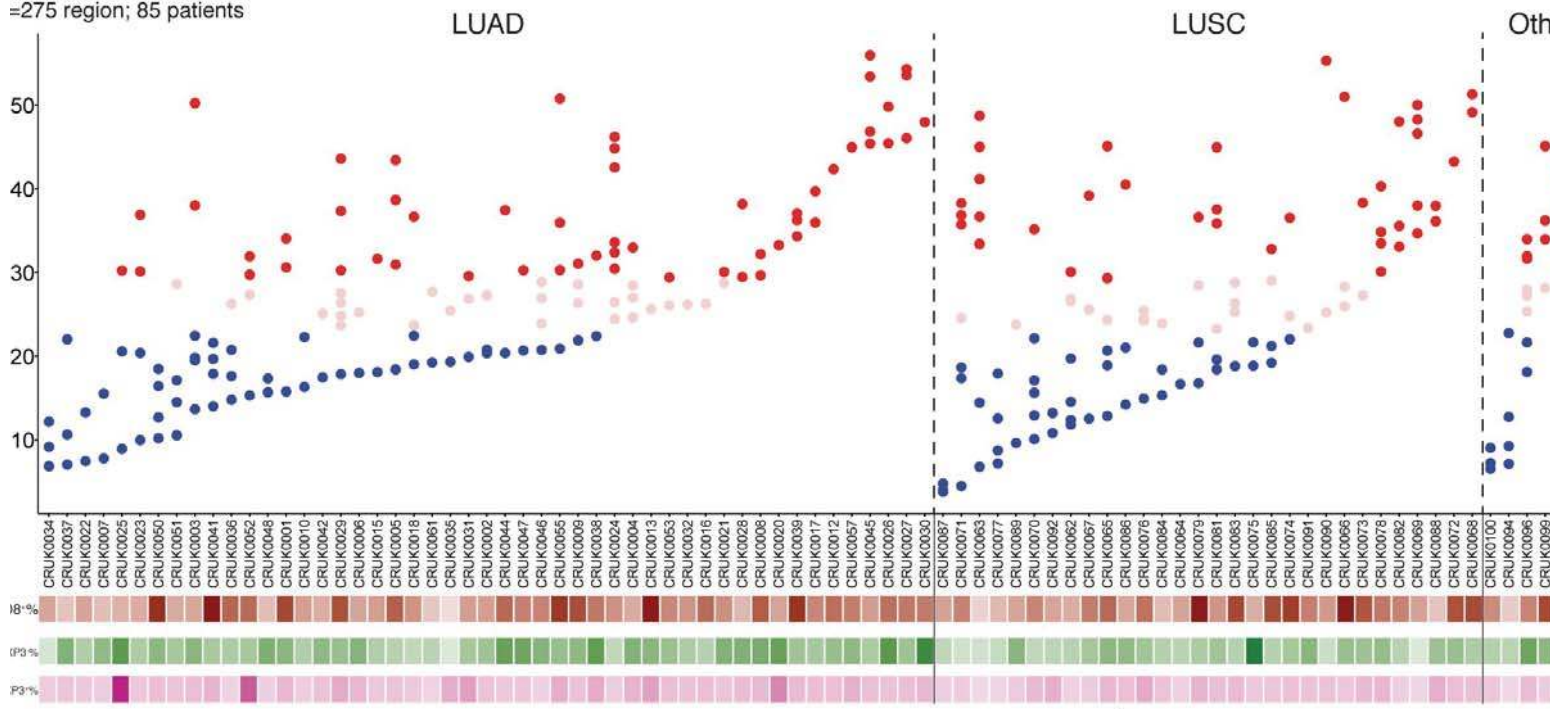
- 1217 (6) Department of Cellular Pathology, University College London, University College Hospital,
1218 London, UK
- 1219 (7) Translational Immune Oncology Group, Centre for Molecular Medicine, Royal Marsden
1220 Hospital NHS Trust, London, UK
- 1221 (8) Department of Pathology, GZA-ZNA-Ziekenhuizen, Antwerp, Belgium
- 1222 (9) Division of Research, Peter MacCallum Cancer Centre, University of Melbourne,
1223 Melbourne, Victoria, Australia
- 1224 (10) MRC Toxicology Unit, Lancaster Road, University of Cambridge, Leicester, UK
- 1225 (11) Leicester Cancer Research Centre, University of Leicester, Leicester, UK
- 1226 (12) Cancer Research UK & University College London Cancer Trials Centre, University College
1227 London, London, UK
- 1228 (13) Cancer Immunology Unit, University College London Cancer Institute, London, UK
- 1229 (14) Cancer Genome Evolution Research Group, University College London Cancer Institute,
1230 University College London, London, UK
- 1231 (15) Glenfield Hospital, University Hospitals Leicester NHS Trust, Groby Road, Leicester, UK
- 1232 (16) Cancer Research Centre, University of Leicester, Leicester, United Kingdom
- 1233 (17) The Francis Crick Institute, London, United Kingdom
- 1234 (18) University College London Cancer Institute, London, United Kingdom
- 1235 (19) Aberdeen Royal Infirmary, Aberdeen, United Kingdom
- 1236 (20) Ashford and St Peter's Hospitals NHS Foundation Trust
- 1237 (21) Barnet & Chase Farm Hospitals, United Kingdom
- 1238 (22) Barts Health NHS Trust
- 1239 (23) Berlin Institute for Medical Systems Biology, Max Delbrueck Center for Molecular Medicine,
1240 Berlin, Germany
- 1241 (24) German Cancer Consortium (DKTK), partner site Berlin
- 1242 (25) German Cancer Research Center (DKFZ), Heidelberg
- 1243 (26) Cancer Research UK Manchester Institute, University of Manchester, Manchester, UK
- 1244 (27) Cancer Research UK Lung Cancer Centre of Excellence, University of Manchester,
1245 Manchester, UK
- 1246 (28) Leicester University Hospitals, Leicester, United Kingdom
- 1247 (29) Cardiff & Vale University Health Board, Cardiff, Wales
- 1248 (30) Christie NHS Foundation Trust, Manchester, United Kingdom

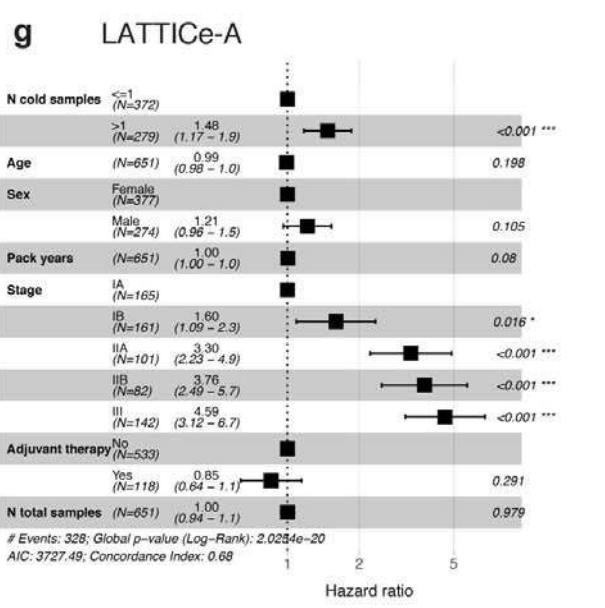
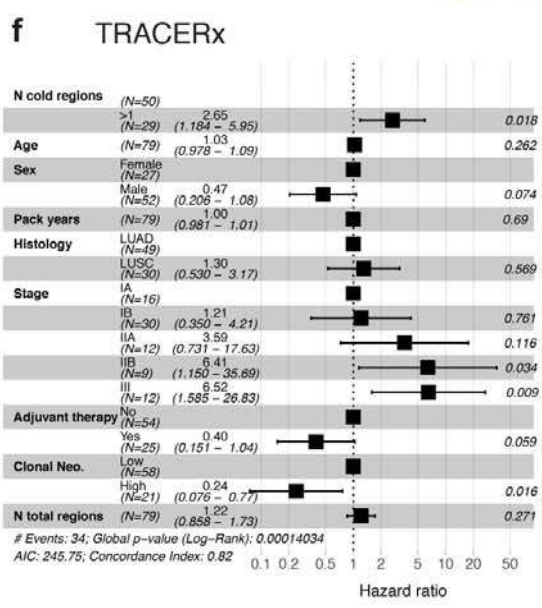
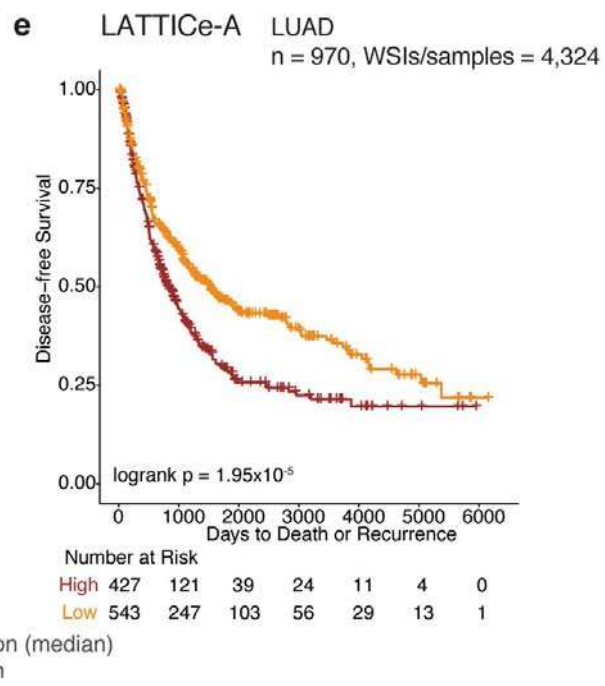
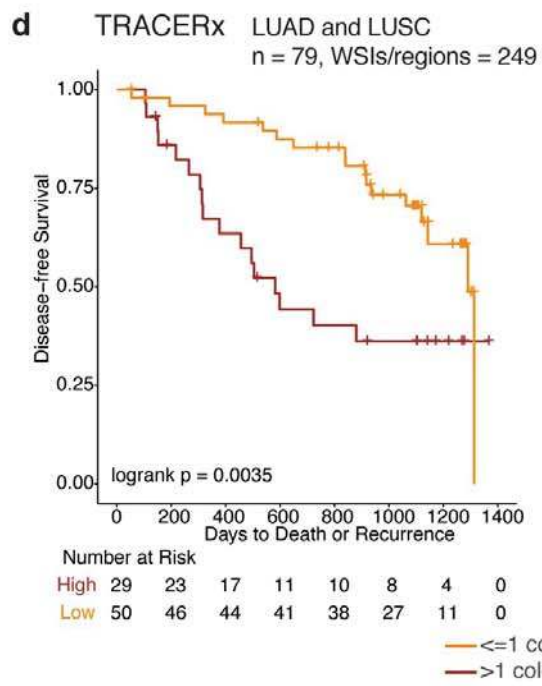
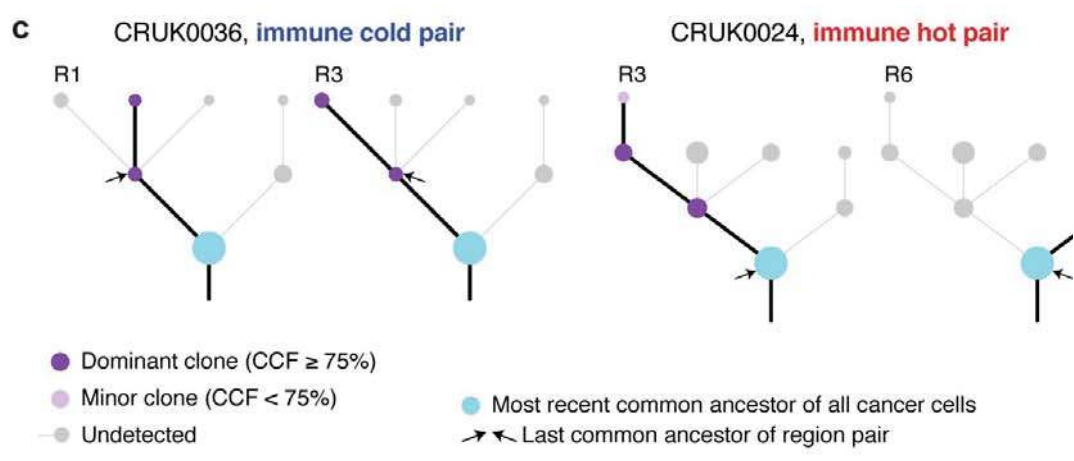
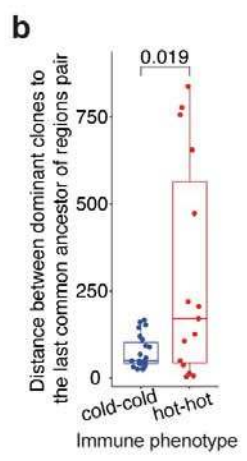
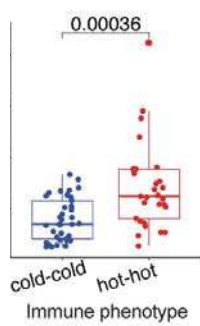
- 1249 (31) Danish Cancer Society Research Center, Copenhagen, Denmark
- 1250 (32) Department of Physics of Complex Systems, ELTE Eötvös Loránd University, Budapest,
1251 Hungary
- 1252 (33) Departments of Radiation Oncology and Radiology, Dana Farber Cancer Institute, Brigham
1253 and Women’s Hospital, Harvard Medical School, Boston, MA, USA
- 1254 (34) Department of Radiology, Netherlands Cancer Institute, Amsterdam, The Netherlands
- 1255 (35) Golden Jubilee National Hospital
- 1256 (36) Independent Cancer Patients Voice
- 1257 (37) University of Leicester, Leicester, United Kingdom
- 1258 (38) Liverpool Heart and Chest Hospital NHS Foundation Trust
- 1259 (39) Royal Liverpool University Hospital
- 1260 (40) Manchester Cancer Research Centre Biobank, Manchester, United Kingdom
- 1261 (41) National Institute for Health Research Leicester Respiratory Biomedical Research Unit,
1262 Leicester, United Kingdom
- 1263 (42) NHS Greater Glasgow and Clyde
- 1264 (43) Royal Brompton and Harefield NHS Foundation Trust
- 1265 (44) Sheffield Teaching Hospitals NHS Foundation Trust
- 1266 (45) The Princess Alexandra Hospital NHS Trust
- 1267 (46) The Whittington Hospital NHS Trust, London, United Kingdom
- 1268 (47) University College London Hospitals, London, United Kingdom
- 1269 (48) University Hospital Birmingham NHS Foundation Trust, Birmingham, United Kingdom
- 1270 (49) University Hospital Southampton NHS Foundation Trust
- 1271 (50) Velindre Cancer Centre, Cardiff, Wales
- 1272 (51) Wythenshawe Hospital, Manchester University NHS Foundation Trust
- 1273 (52) Division of Infection, Immunity and Respiratory Medicine, University of Manchester,
1274 Manchester, UK
- 1275

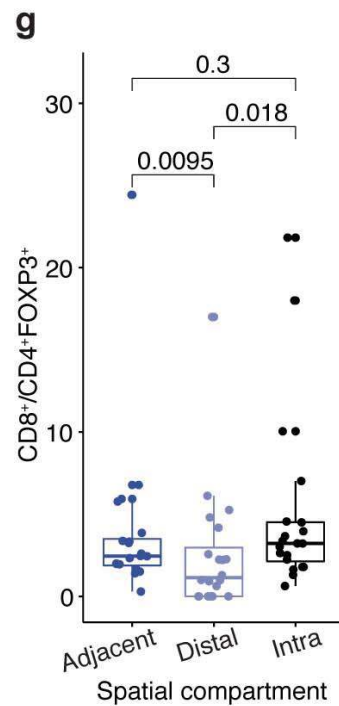
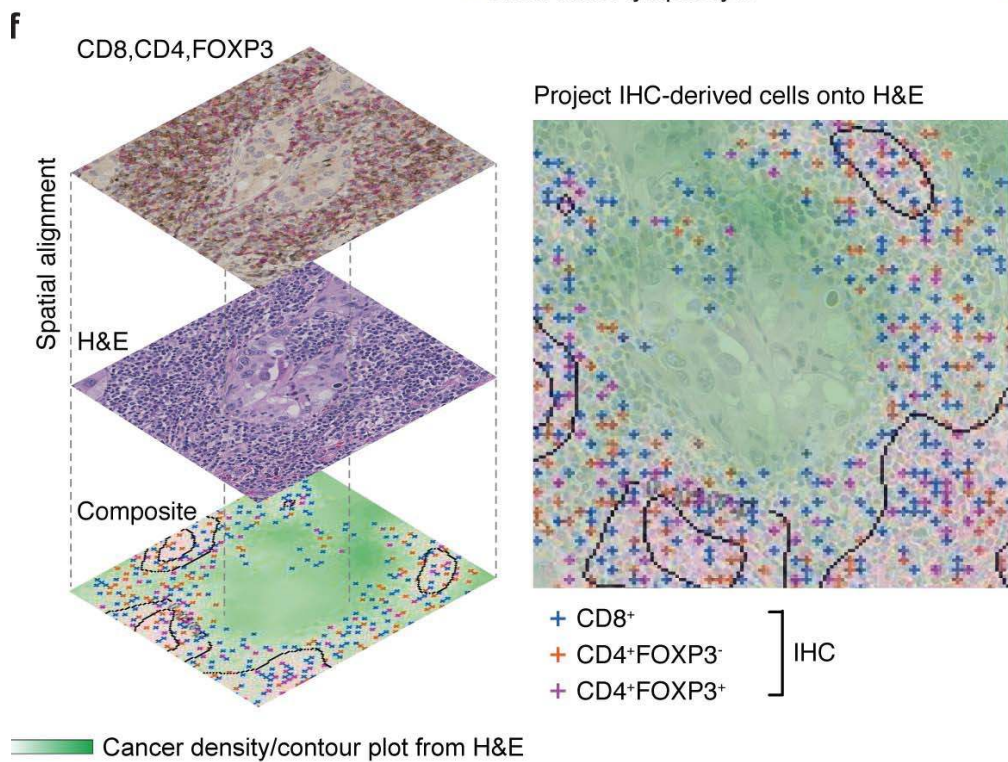
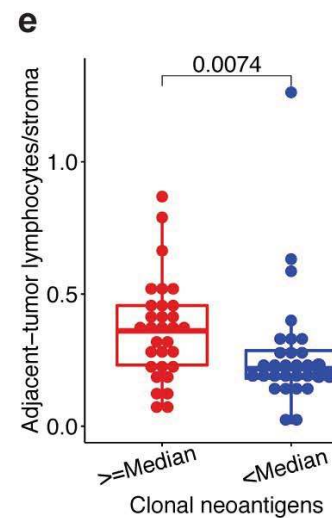
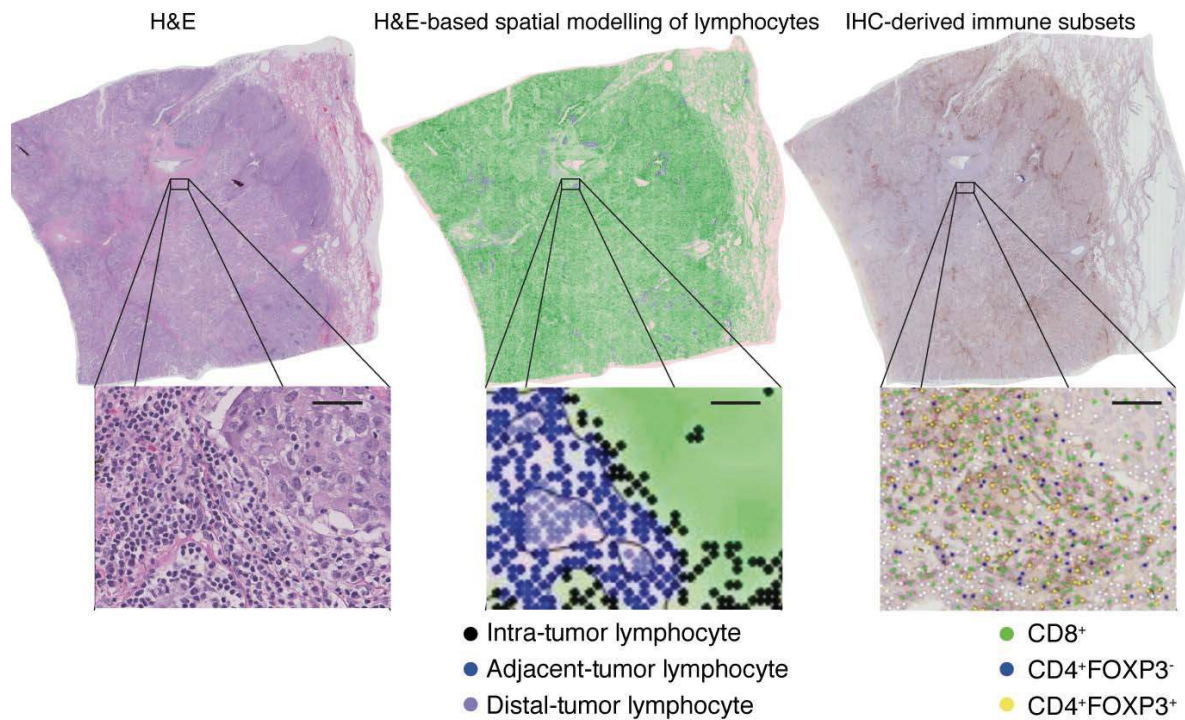
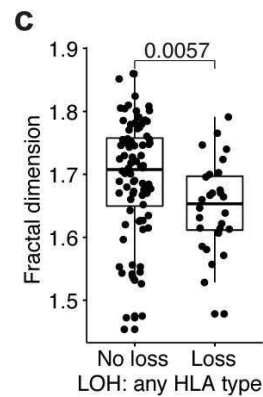
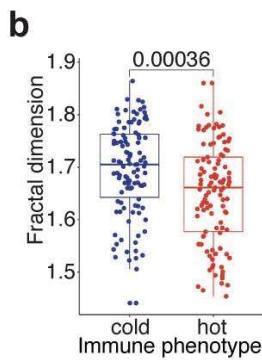
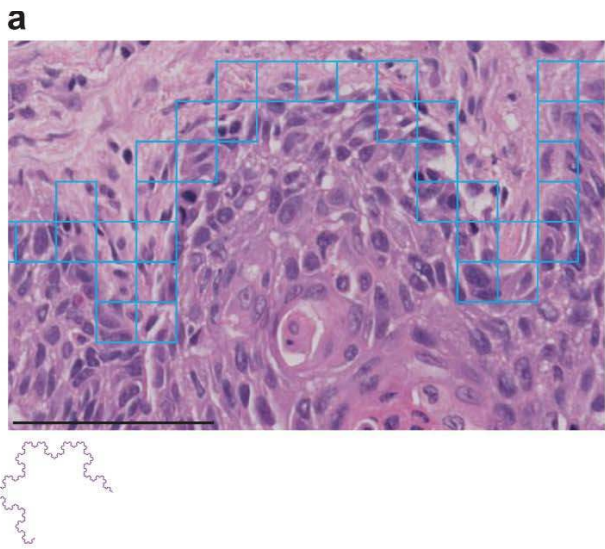




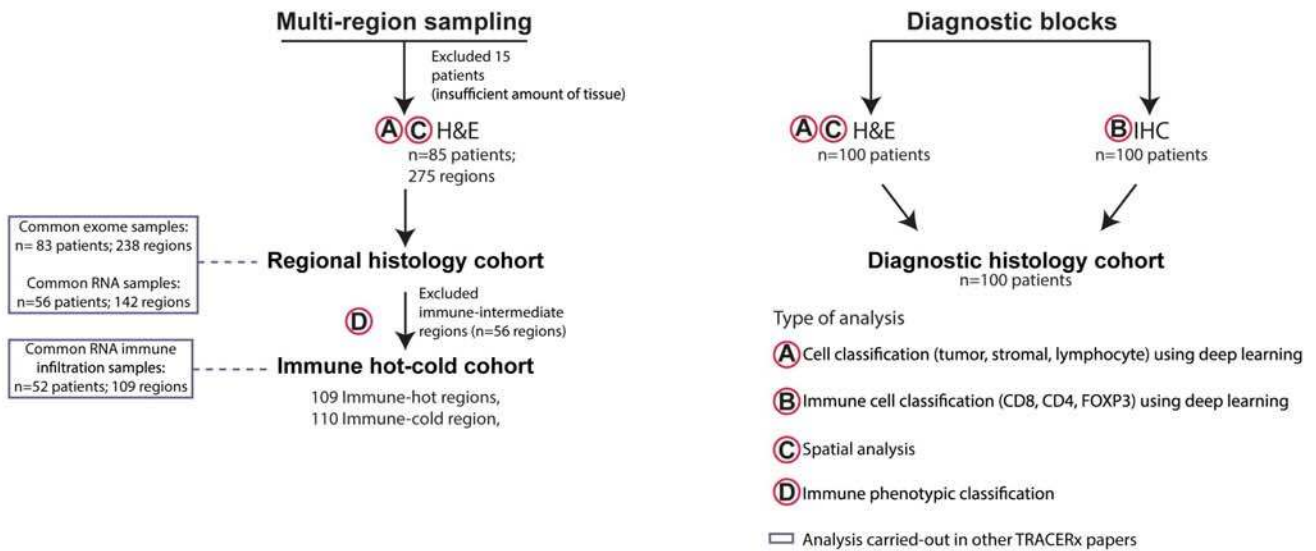
=275 region; 85 patients



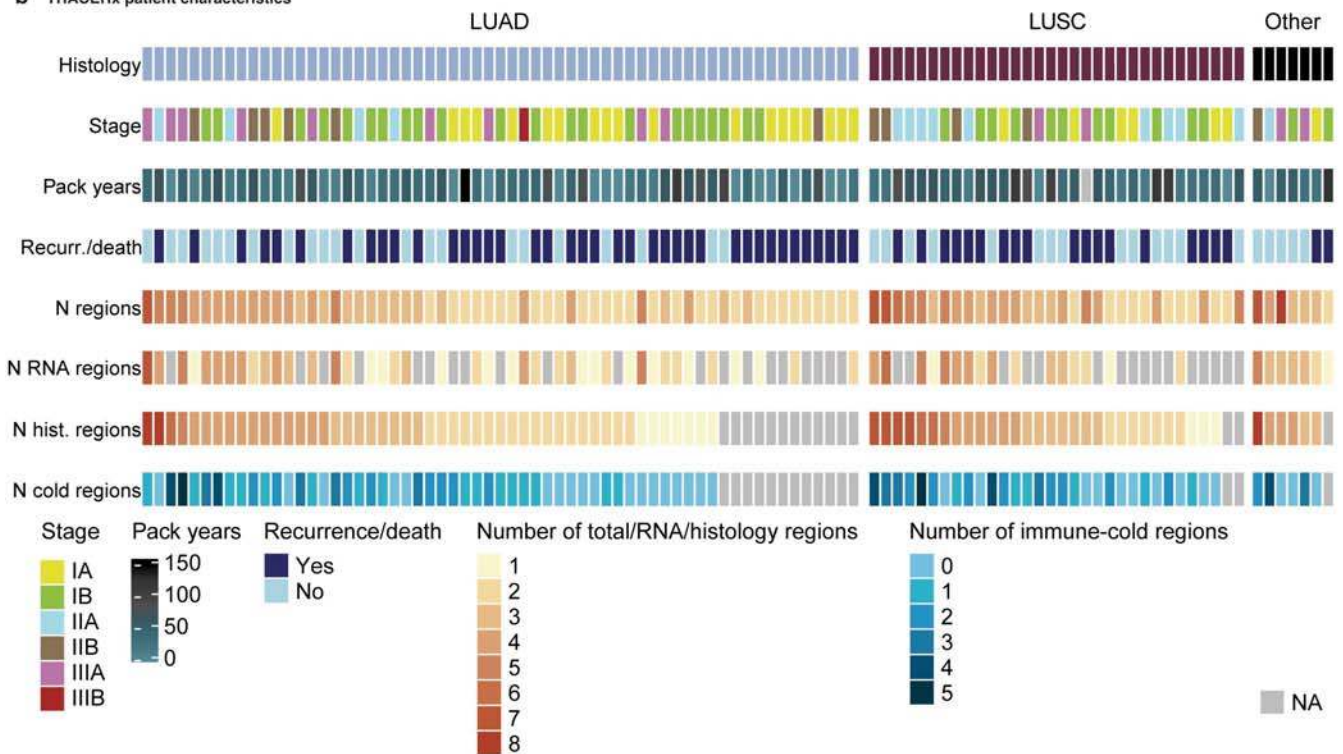




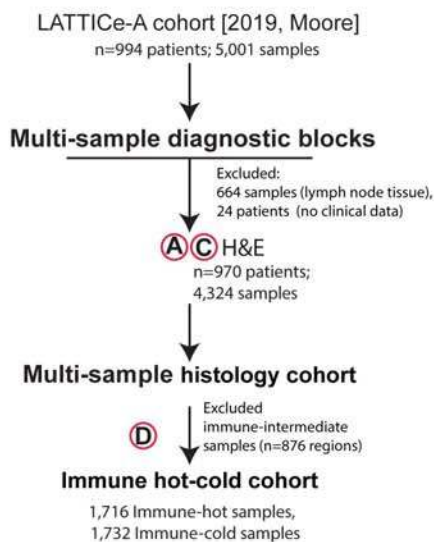
TRACERx 100 patient cohort [2017, Jamal-Hanjani]
n=100 patients; 303 regions



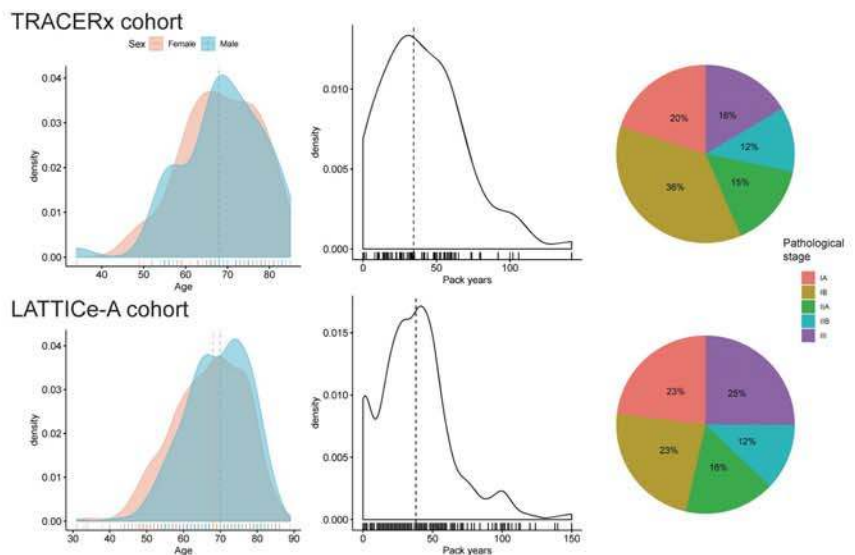
b TRACERx patient characteristics



c Validation CONSORT diagram

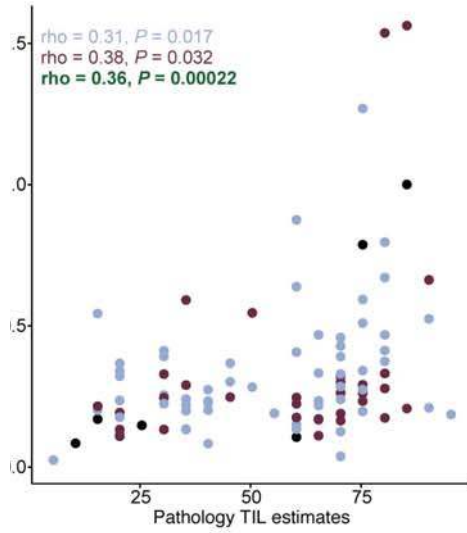


d Demographic and clinical overview

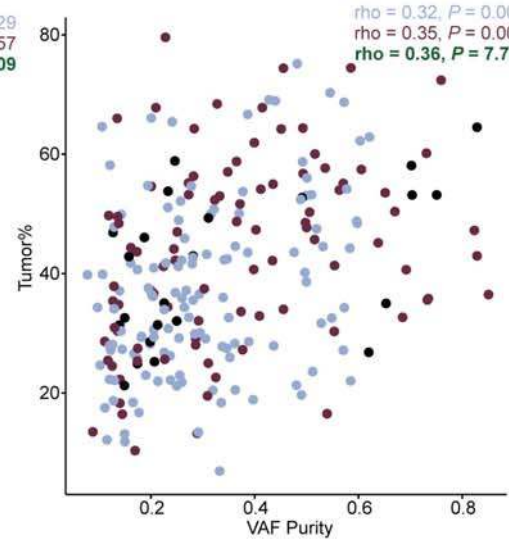
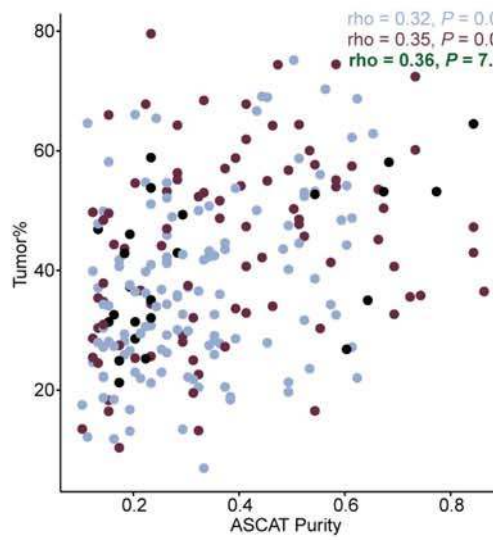


● LUAD
● LUSC
● Other

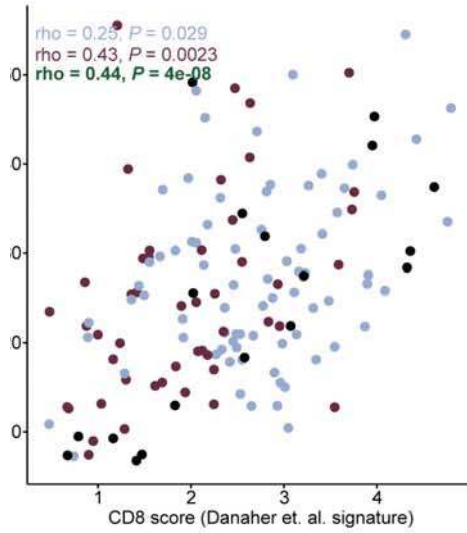
a TRACERx, diagnostic samples (n=98)



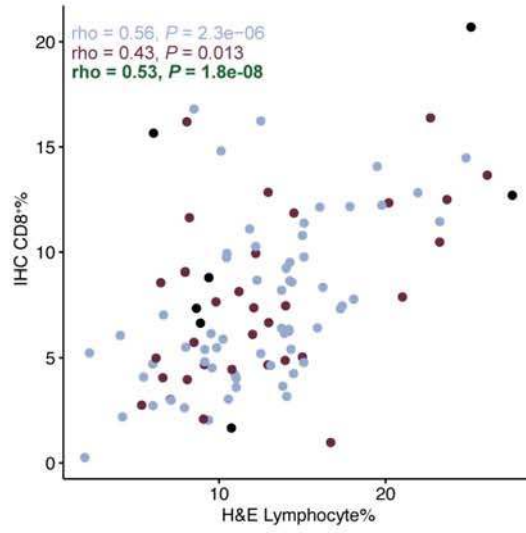
b TRACERx, regional histology and CNA samples (n=238)



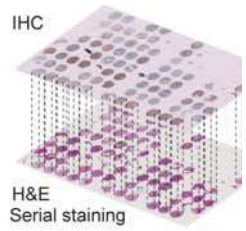
c TRACERx, regional histology and RNA-seq samples (n=142)



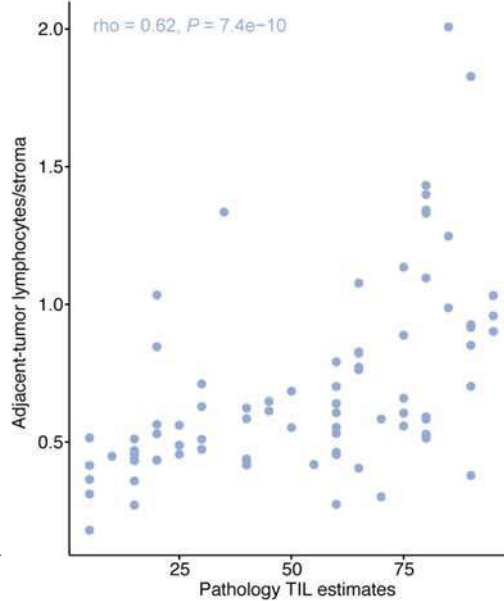
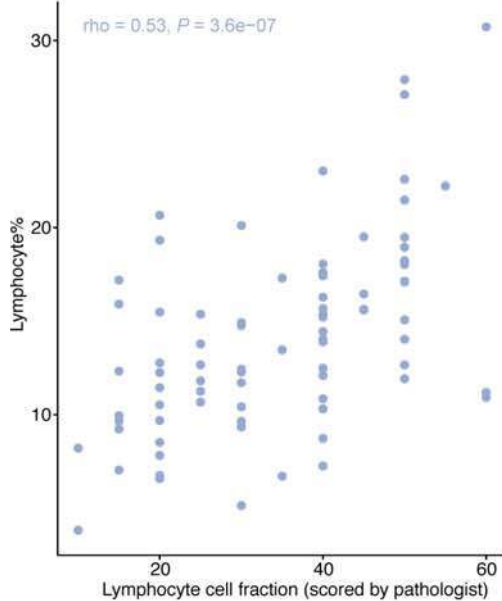
d TRACERx, diagnostic samples (n=100)



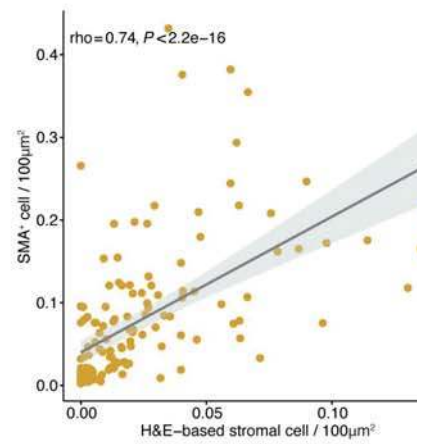
f

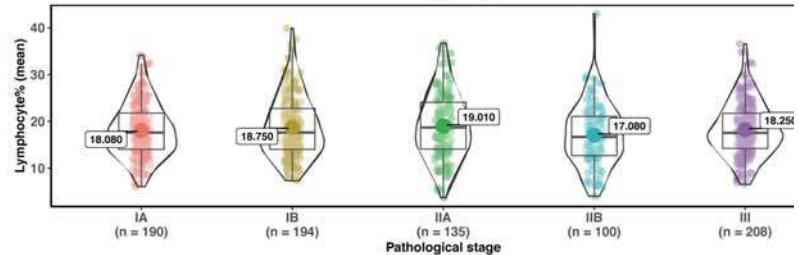
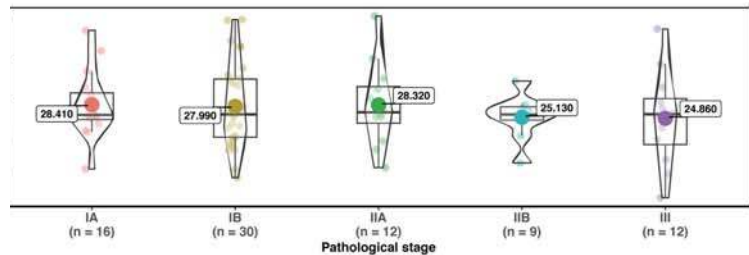
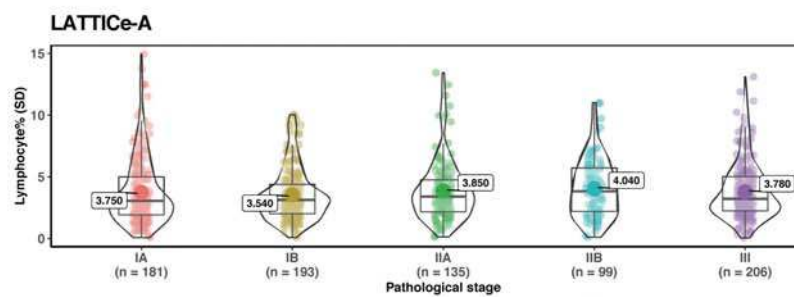
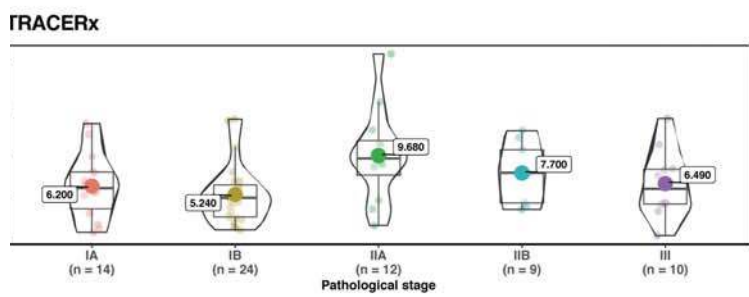
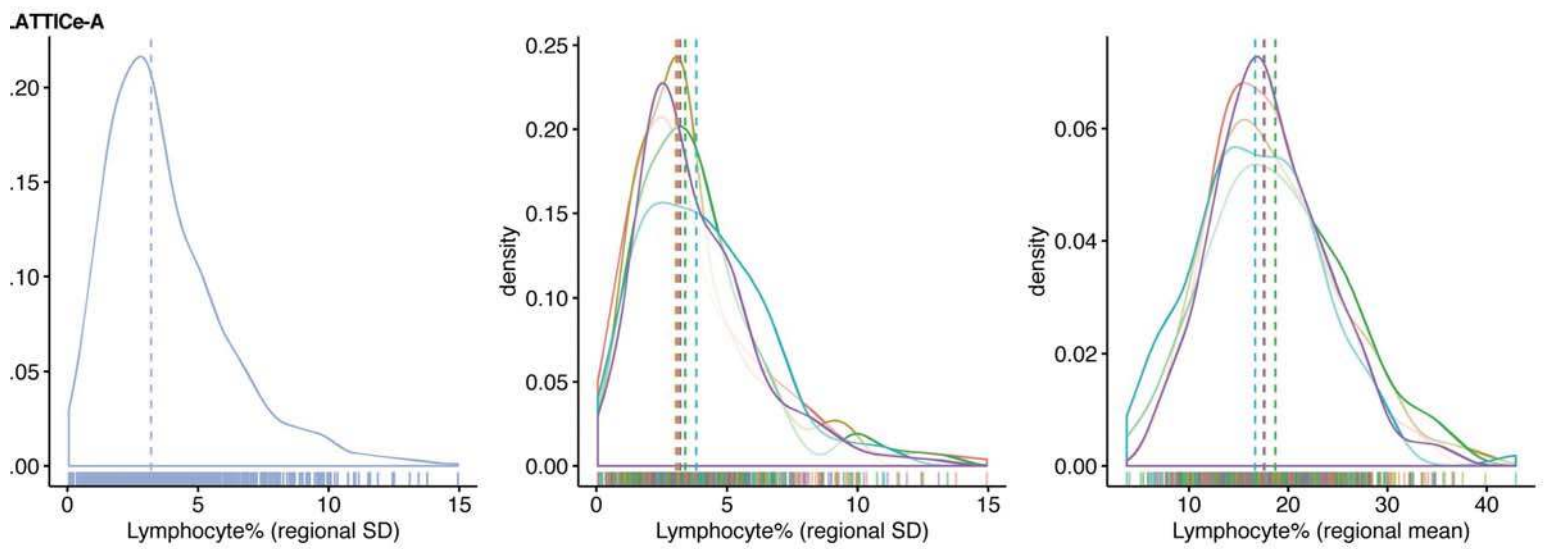
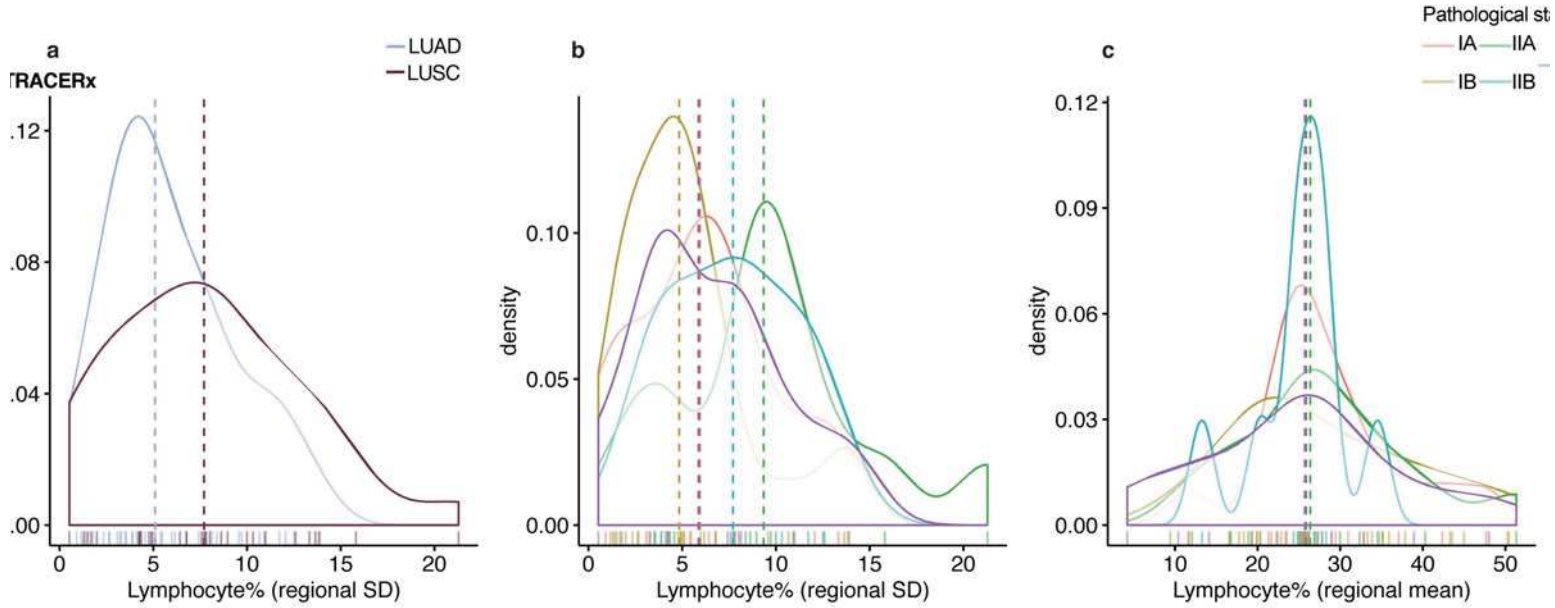


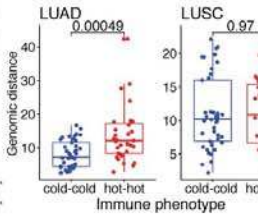
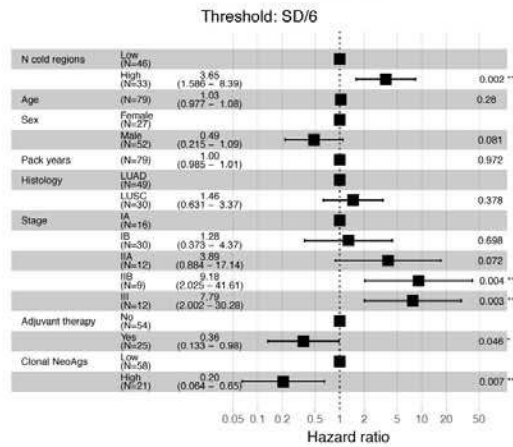
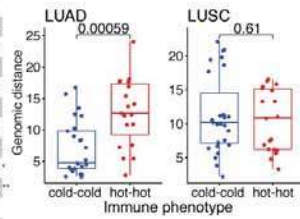
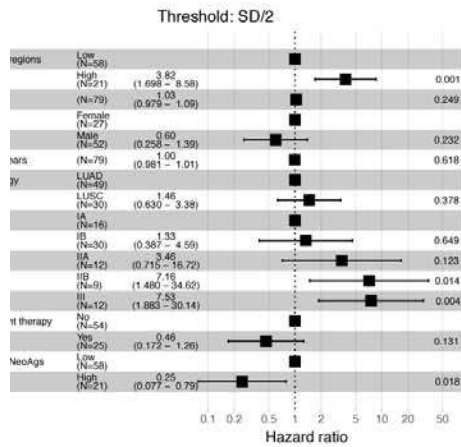
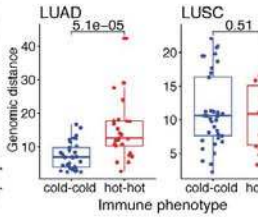
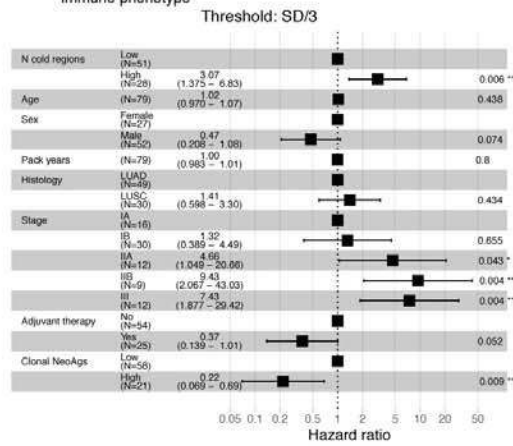
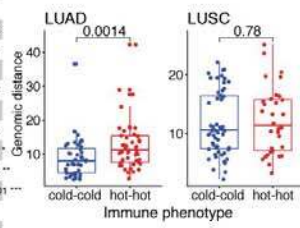
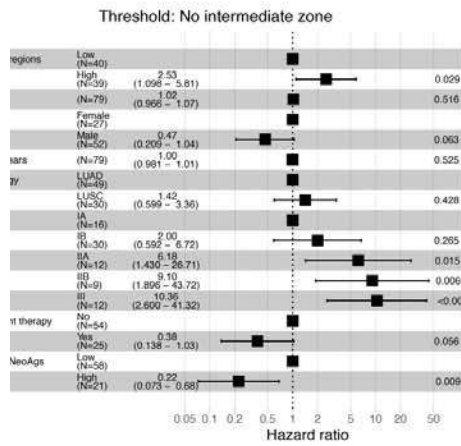
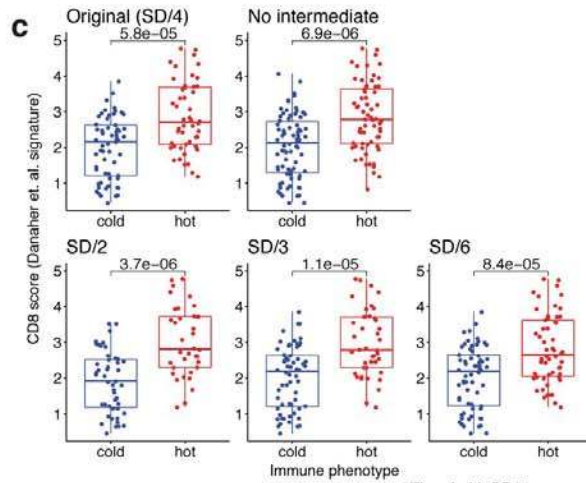
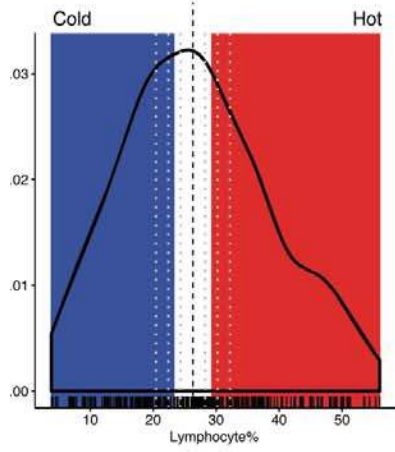
e LATTICE-A, diagnostic samples (n=80)



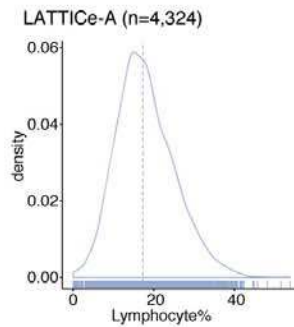
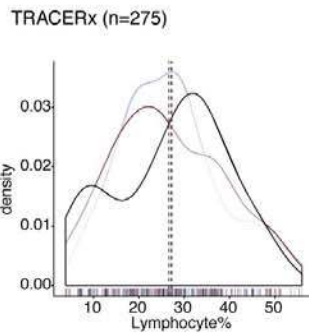
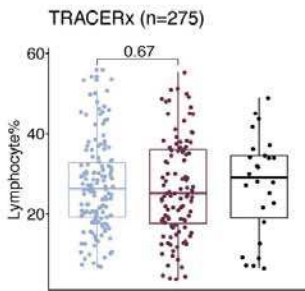
g



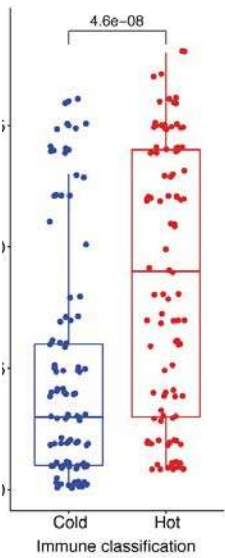




J



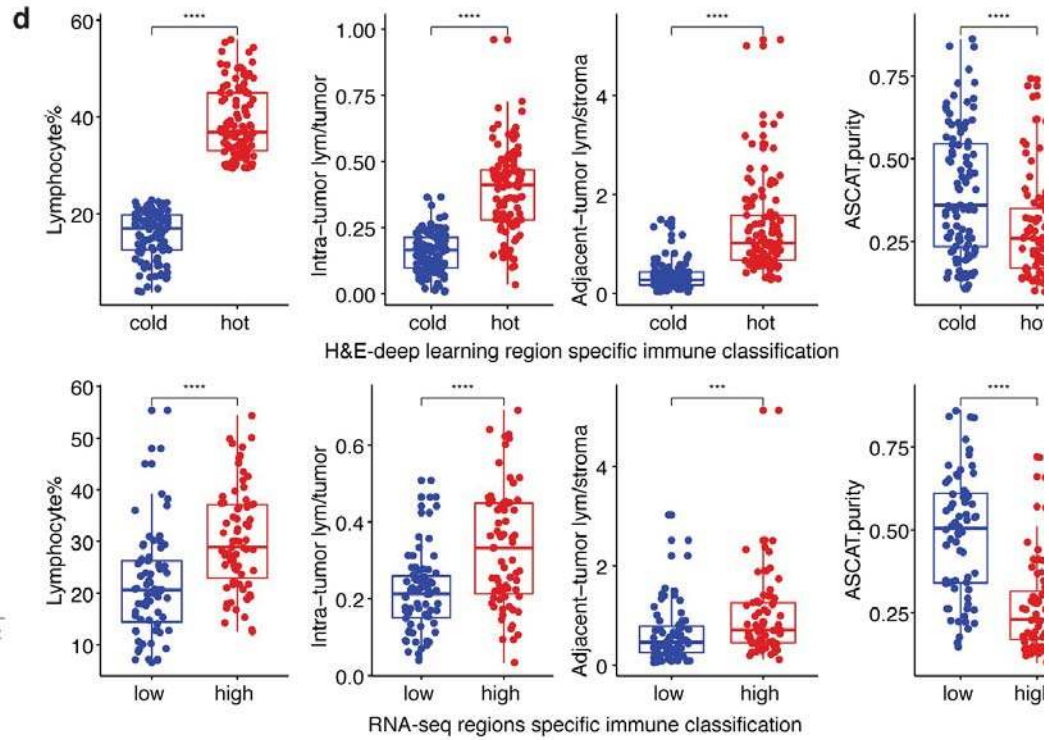
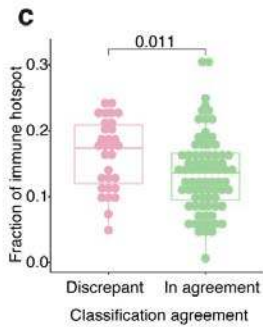
— LUAD
— LUSC
— Other

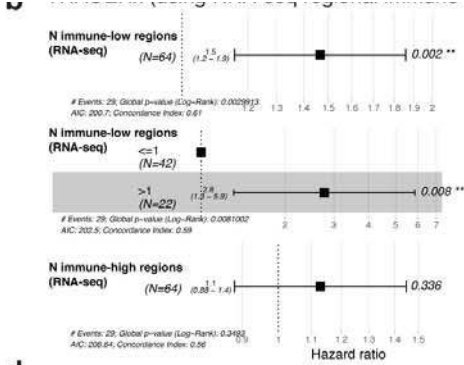
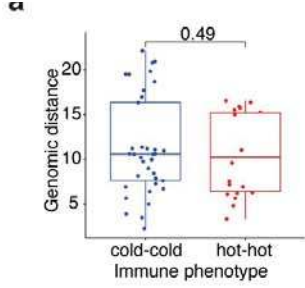


b

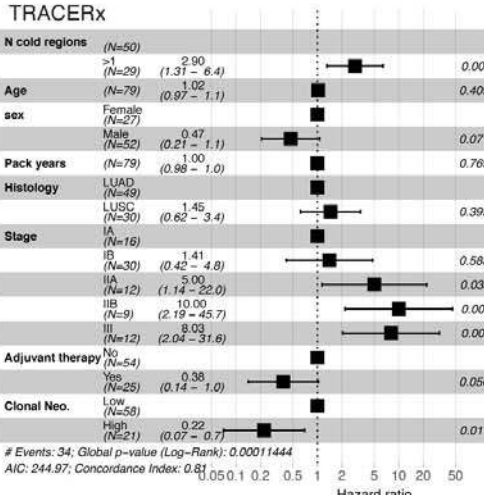
		Deep learning	
		Hot	Cold
RNA-seq	High	35	18
	Low	13	43

p=7.8e-06

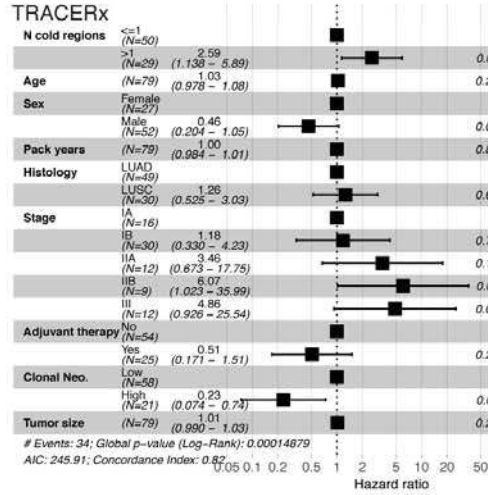




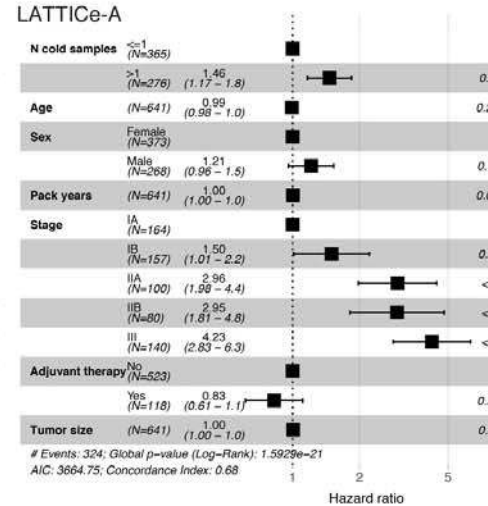
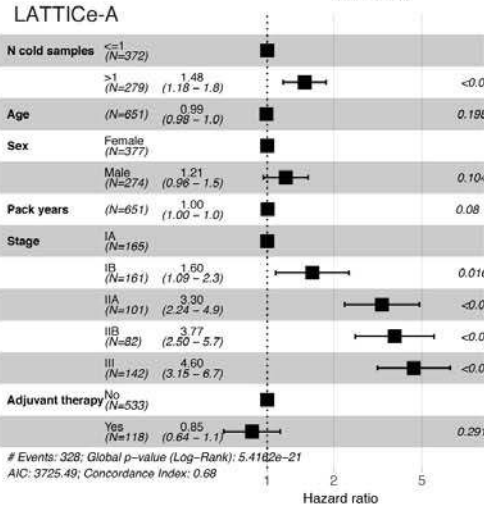
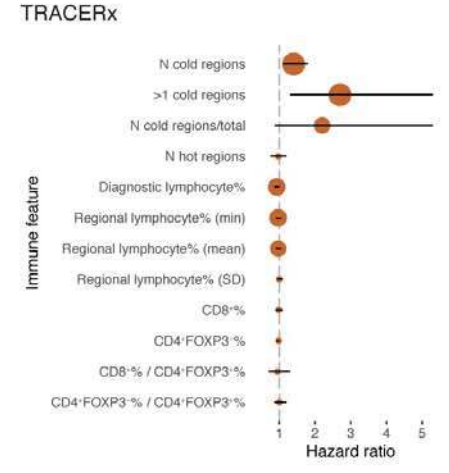
C Multivariate analysis



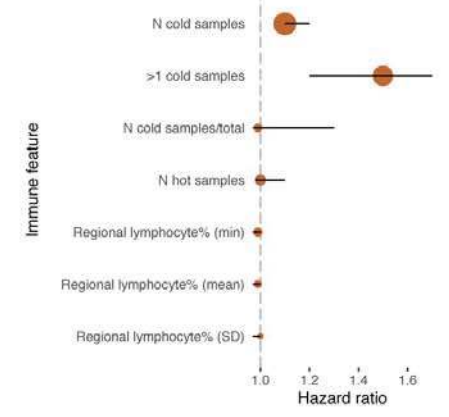
d Multivariate analysis (including tumor size)



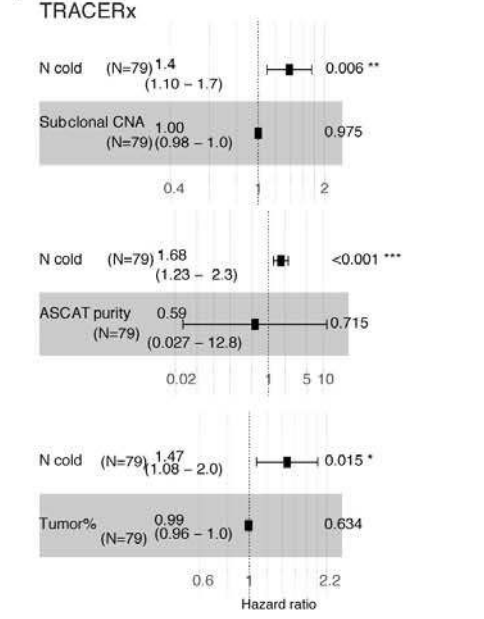
e



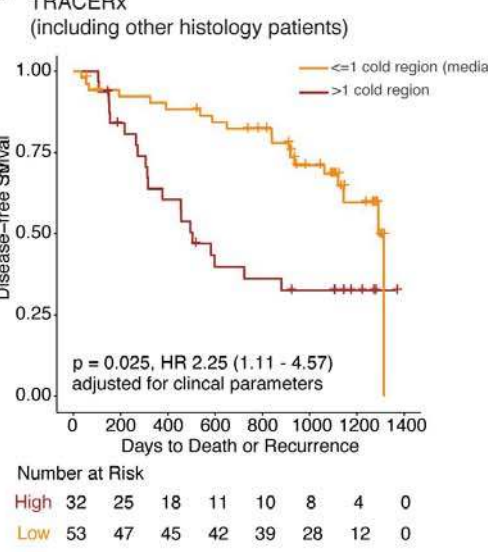
LATTICE-A



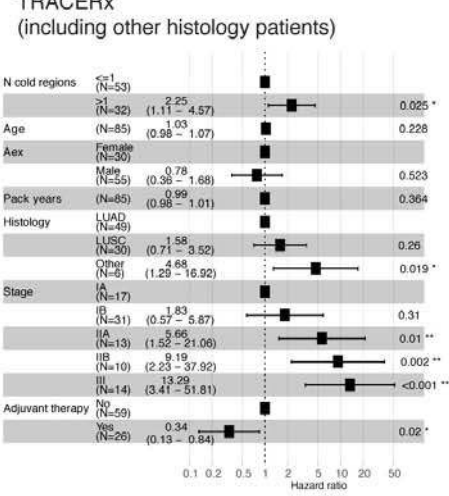
f

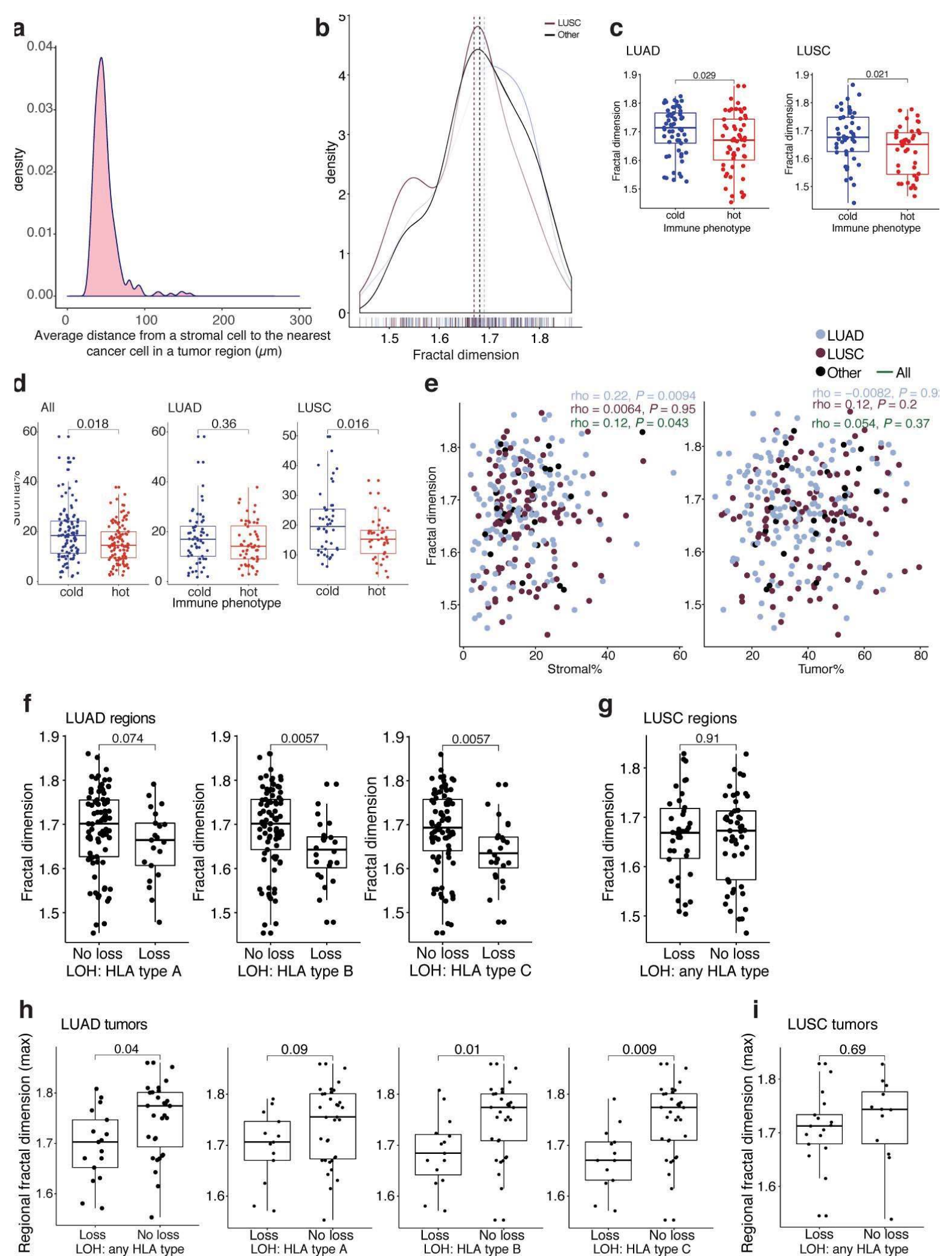


g



h





CD8 ⁺ /CD4 ⁺ FOXP3 ⁺					
CD8 ⁺ %	0.13				0.11
CD4 ⁺ FOXP3 ⁺ %		-0.17			
ITLR	0.19	0.16		0.19	0.22
Adjacent tumor lym/stroma	0.37*	0.19		0.15	
Lymphocyte%	0.3	0.2	0.16	0.13	0.16
	Clonal neo.	Subclonal neo.	HLA LOH-A	HLA LOH-B	HLA LOH-C

